SANDIA REPORT

SAND2011-8527
Unlimited Release
October 2011

Fast Neutron Environments

Khalid Hattar, Luke N. Brewer, Brad L. Boyce, Thomas E. Buchheit, Stephen M. Foiles, Ping Lu, Blythe G. Clark, Paul G. Kotula, Steven Goods, Joseph Puskar, and Barney L. Doyle

Prepared by
Sandia National Laboratories
Albuquerque, New Mexico 87185 and Livermore, California 94550

Sandia National Laboratories is a multi-program laboratory managed and operated by Sandia Corporation,
a wholly owned subsidiary of Lockheed Martin Corporation,
for the U.S. Department of Energy's National Nuclear Security Administration
under contract DE-AC04-94AL85000.

Approved for public release; further dissemination unlimited.

Sandia National Laboratories

Issued by Sandia National Laboratories, operated for the United States Department of Energy by Sandia Corporation.

NOTICE: This report was prepared as an account of work sponsored by an agency of the United States Government. Neither the United States Government, nor any agency thereof, nor any of their employees, nor any of their contractors, subcontractors, or their employees, make any warranty, express or implied, or assume any legal liability or responsibility for the accuracy, completeness, or usefulness of any information, apparatus, product, or process disclosed, or represent that its use would not infringe privately owned rights. Reference herein to any specific commercial product, process, or service by trade name, trademark, manufacturer, or otherwise, does not necessarily constitute or imply its endorsement, recommendation, or favoring by the United States Government, any agency thereof, or any of their contractors or subcontractors. The views and opinions expressed herein do not necessarily state or reflect those of the United States Government, any agency thereof, or any of their contractors.

Printed in the United States of America. This report has been reproduced directly from the best available copy.

Available to DOE and DOE contractors from
U.S. Department of Energy
Office of Scientific and Technical Information
P.O. Box 62
Oak Ridge, TN 37831

Telephone: (865) 576-8401
Facsimile: (865) 576-5728
E-Mail: reports@adonis.osti.gov
Online ordering: http://www.osti.gov/bridge

Available to the public from
U.S. Department of Commerce
National Technical Information Service
5285 Port Royal Rd.
Springfield, VA 22161

Telephone: (800) 553-6847
Facsimile: (703) 605-6900
E-Mail: orders@ntis.fedworld.gov
Online order: http://www.ntis.gov/help/ordermethods.asp?loc=7-4-0#online

SAND2011-8527
Unlimited Release
October 2011

Fast Neutron Environments

Khalid Hattar, Blythe G. Clark, and Barney L. Doyle
01111
Thomas E. Buchheit, Stephen M. Foiles,
01814
Ping Lu, Paul G. Kotula. J.D. Puskar
01822
Brad L. Boyce
01831
Steven Goods
08252
Sandia National Laboratories
P.O. Box 5800
Albuquerque, New Mexico 87185-1056

Luke N. Brewer
Department of Mechanical and Aerospace Engineering
Graduate School of Engineering and Applied Sciences
Naval Postgraduate School
Monterey, CA 93943

Abstract

The goal of this LDRD project is to develop a rapid first-order experimental procedure for the testing of advanced cladding materials that may be considered for generation IV nuclear reactors. In order to investigate this, a technique was developed to expose the coupons of potential materials to high displacement damage at elevated temperatures to simulate the neutron environment expected in Generation IV reactors. This was completed through a high temperature high-energy heavy-ion implantation. The mechanical properties of the ion irradiated region were tested by either micropillar compression or nanoindentation to determine the local properties, as a function of the implantation dose and exposure temperature. In order to directly compare the microstructural evolution and property degradation from the accelerated testing and classical neutron testing, 316L, 409, and 420 stainless steels were tested. In addition, two sets of diffusion couples from 316L and HT9 stainless steels with various refractory metals. This study has shown that if the ion irradiation size scale is taken into consideration when developing and analyzing the mechanical property data, significant insight into the structural properties of the potential cladding materials can be gained in about a week.

ACKNOWLEDGMENTS

The authors would like to thank Dan Buller and Stuart Van Deusen for their time and expertise needed to complete the high temperature ion implantations. The authors would also like to thank Stuart Maloy, Andrew T. Nelson, and Osman Anderoglu for the many useful discussions and for supplying the HT9 steel used to produce the diffusion couples. The authors would also like to thank Peter Hosemann from University of California, Berkeley, Mitra Taheri from Drexel University, Mark Kirk from Argonne National Laboratory, Emmanuelle Marques from University of Michigan, and Yong Q. Wang from Los Alamos National Laboratory.

CONTENTS

1. Introduction 11
1.1. Principles of Accelerated Testing of Cladding Materials 11
2. Rapid Displacement Damage through High Temperautre Ion Irradiation 13
3. Proof of Concept 17
3.1. High-Energy Heavy-Ion Irradiation Conditions 17
3.2. Micropillar Compression Production 19
3.3. Individual Micropillar Irradiation 26
4. Qualification of Technique in Stainless Steel 28
4.1. Finite Element Modeling of Nanoindentation into Irradiated Steels 28
4.2. Sample Preparation Ion Irradiation Conditions 29
4.3. Spherical Nanoindentation Results 29
4.4. Berkovich Nanoindentation Results 31
4.5. Microstructural Examination of Irradiated Region 35
5. Extension of Acelerated Testing to Diffusion Couples 42
5.1. Production of Diffusion Couples 42
5.2. Compositional Characterization of Diffusion Couples 43
5.3. Initial Nanoindentation Testing of Diffusion Couples 48
5.4. High-Energy Heavy-Ion Irradiation Conditions 51
5.5. Nanoindentation Testing of Irradiated Diffusion Couples 51
6. Nearly In-situ Scanning Electron Microscopy / Electron Backscattered Diffraction Technique 55
6.1. Nearly In-situ SEM/EBSD System Configuration 55
6.2. Preliminary Results in an Iconel Alloy 56
7. In-situ Ion Irradiation Transmission Electron Microscopy Technique 57
7.1. Need to Understand Structural Evolution at the Nanoscale 57
7.2. History of In-situ Ion Irradiation TEM 57
7.3. In-situ Ion Irradiation TEM System Configuration 58
7.4. Preliminary Results 63
7.5. Future Direction and Planned Collaborations 64
8. Conclusions 67
9. References 69
Distribution 71

FIGURES

Figure 1. Three potential Generation IV reactors: super critical water cooled reactor, sodium cooled fast reactor, and the molten salt reactor..... 11
Figure 2. Ion damage simulation demonstrating the effect of the atomic number of the ion upon the damage rate at nominally room temperature..... 13
Figure 3. A plot of the irradiation damage as a function of depth in stainless steel and a schematic of the various defect structures that might result from ion implantation..... 14
Figure 4. Button heater with thermocouples used for *in situ* heating experiments..... 15
Figure 5. Control of temperature for *in situ* heating during ion implantation 16
Figure 6. SRIM simulations of ion scattering of 20 MeV nickel into stainless steel. Note that the mean ion range from this simulation is 3.6μm..... 18
Figure 7. Compositional traces from STEM-EDX line profiles across copper implanted and pristine steel surfaces. A.) compositional traces, B.) annular dark field image from e-brite steel. 19
Figure 8. SEM micrographs of pristine and irradiated ebrite steel (Fe-26Cr-1Mo) using a 30MeV copper ion beam at room temperature. (experiment performed at SNL) Note the pronounced phase separation in these backscattered electron images..... 19
Figure 9. An array of micropillars created in single crystal Cu by FIB..... 20
Figure 10 Two micropillars both milled to have 2:1::Height:Diameter ratio..... 21
Figure 11. Stress strain curves from the control and irradiated 10 µm tall pillars..... 22
Figure 12. Deformed pillars after compression of the irradiated and controlled 10 µm tall pillars 23
Figure 13. Stress strain curves from the control and irradiated 5 µm tall pillars..... 24
Figure 14. Deformed pillars after compression of the irradiated and controlled ? µm tall pillars. 24
Figure 15. Stress strain curves from the control and irradiated 4 µm tall pillars..... 25
Figure 16. Deformed pillars after compression of the irradiated and controlled 4 µm tall pillars. 26
Figure 17. SEM images of irradiation damage of select pillars in within an array 26
Figure 18. SEM images of irradiation damage of select pillars in within an array 27
Figure 19.Finite Element Model of conical indentation of a control and a irradiation hardened microstructure 28
Figure 20. Simulated Hardness for both conical and spherical nanoindenters based on FEM simulation..... 29
Figure 21. Schematic indicating the advantages of spherical indentation to provide information on the active creep mechanism 30
Figure 22. Hardness as a function of depth for spherical indentations at 400 ºC, 500ºC, and 600ºC..... 30
Figure 23. Optical Micrograph of an array of Berkovick indentations in steel 31
Figure 24. Nanoindentation results of controlled regions and irradiated regions to approximately 10 dpa at 400 ºC, 500ºC, and 600ºC 32
Figure 25. Nanoindentation results of controlled regions and irradiated regions to approximately 40 dpa at 400 ºC, 500ºC, and 600ºC 32
Figure 26. Nanoindentation results of controlled regions and irradiated regions to approximately 100 dpa at 400 ºC, 500ºC, and 600ºC 33

Figure 27. Nanoindentation results of controlled regions and irradiated regions to approximately 10 dpa, 40dpa, and 100 dpa at 400 ºC, 500ºC, and 600ºC 34
Figure 28. Nanoindentation results of controlled regions and irradiated regions. The samples were irradiated at various ion fluxes. 35
Figure 29. EBSD orientation map of 316L control and 100 dpa irradiated regions. 36
Figure 30. Pole figures of 316L control and 100 dpa irradiated regions. 37
Figure 31. TEM micrograph of the 316L 100 dpa 600 ºC irradiated region as a function of depth. 38
Figure 32. TEM micrographs taken at 1.5 µm into the coupon illustrating the effects of ion irradiation temperature and dose on microstructure. 39
Figure 33. STEM micrograph and EDS maps of the 316L 100 dpa 500 ºC and 600 ºC irradiated region. 40
Figure 34. STEM micrograph of the 316L 100 dpa 600 ºC irradiated region and accompaning EDS spectra. 40
Figure 35. Photograph of the 316L diffusion couple set and a schematic of what the 43
Figure 36. WDS scan and SEM image of the tungsten 316L stainless steel interface 44
Figure 37. WDS scan and SEM image of the tantalum 316L stainless steel interface 45
Figure 38. WDS scan and SEM image of the molybdenum 316L stainless steel interface 46
Figure 39. WDS scan and SEM image of the niobium316L stainless steel interface 47
Figure 40. Nanoindentation results across the tantalum 316L stainless steel diffusion couple interface 48
Figure 41. Nanoindentation results across the niobium 316L stainless steel diffusion couple interface 49
Figure 42 SEM image with the different phases formed in the niobium stainless steel diffusion couple interface 50
Figure 43. Optical image of the nanoindentation impressions across the niobium 316L stainless steel diffusion multiple interface 51
Figure 44. Nanoindentation results across a diffusion couple interface 52
Figure 45. Nanoindentation results across a diffusion couple interface 53
Figure 46. Nanoindentation results across a 10 dpa irradiated diffusion couple interface 53
Figure 47. Nanoindentation results across a Ni ion irradiated diffusion couple interface 54
Figure 48. Schematic of the nearly in-situ ion irradiation system on the micro-ONE beam line at the Ion beam Lab 56
Figure 49. Picture of the micro-ONE beam line with the SEM, optical microscope and ion beam line identified. 56
Figure 50. Electron backscattered diffraction pattern and orientation map of a Iconel standard using the EBSD system installed on micro-ONE beam line 57
Figure 51. A map of the location of in-situ ion irradiation TEM facilities around the world 58
Figure 52. The floor plan for the ion beam lab with the location of the new in-situ ion irradiation TEM indicated. 59
Figure 53. Development plans and current status of the In-situ Ion Irradiation TEM 60
Figure 54. PBO simulation of a beam line configuration considered for the in-situ ion irradiation TEM beam line. 61
Figure 55. Schematic of the proposed development of the In-situ Ion Irradiation TEM 61
Figure 56. In-situ Ion Irradiation TEM from vision to completed first generation 62

Figure 57. Images of defect structure evolution in ion irradiated steels performed at IV-TEM and Argonne National Laboratory 64

TABLES

Table 1. A comparison of characteristics of various neutron generating test facilities 11
Table 2. The Matrix of indentation performed on 316L stainless steel 31
Table 3. A set of nanoindentation experiments run on the 420 stainless steel 34

NOMENCLATURE

DOE	Department of Energy
dpa	displacements per atom
EDM	electrical discharge machining
FEM	Finite Element Modeling
FIB	Focused Ion Beam
GNEP	Global Nuclear Energy Partnership
HIP	hot isostatic pressing
IBL	Ion Beam Laboratory
I^3TEM	In-situ Ion Irradiation Transmission Electron Microscopy
LBNL	Lawrence Berkeley National Laboratory
LDRD	Laboratory Directed Research and Development
MTS	Materials Test Station
PBO	Particle Beam Optics
SEM	Scanning Electron Microscopy
SNL	Sandia National Laboratories
SRIM	Stopping and Range of Ions in Matter
STEM	Scanning Transmission Electron Microscopy
TEM	Transmission Electron Microscopy
WDS	wavelength dispersive x-ray spectroscopy

1. INTRODUCTION

1.1. Principles of Accelerated Testing of Cladding Materials

Our country's energy needs are driving a renewed interest in power generation and waste management by reviving fast neutron reactor technology. While promising, fast neutron reactors will drive materials requirements in different directions from the more standard thermal neutron reactors. In order to support programs such as the Global Nuclear Energy Partnership (GNEP), we must find a way to measure, understand, and predict materials properties at high temperatures and under high energy neutron irradiation. However, there are presently no operating fast neutron reactors in the United States. Several types of generation IV reactors are being considered these include, but are not limited to super critical water cooled reactors, sodium cooled fast reactors, and the molten salt reactors. The general design of each can be seen in Figure 1. Each of these reactor designs will require the operation of the reactor cladding materials in environments of greater neutron flux and higher temperatures. Even when fast reactors in the U.S. become operational again, available time for materials experiments on nuclear reactors is in general limited and may not be sufficient for achieving the high levels of damage (100-200 dpa) that are necessary for understanding materials life issues. A means for accelerated testing of irradiation damage in a laboratory environment is clearly necessary in order to develop new cladding materials that can withstand the expected extreme environments.

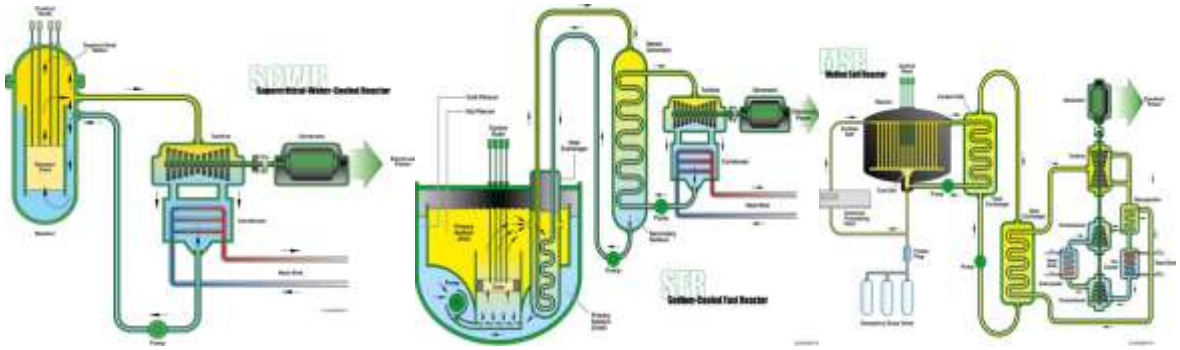

Figure 1. Three potential Generation IV reactors: super critical water cooled reactor, sodium cooled fast reactor, and the molten salt reactor

As is seen in Table 1, the next generation of fast neutron reactors will need materials which can withstand neutron irradiation damage in excess of 100 displacements per atom (dpa). The current irradiation testing capabilities are based primarily on thermal neutron reactors and cannot create more than 20 dpa per year of exposure, leading to test requirements of several years. In addition, the irradiation physics is quite different between thermal neutrons (meV) and fast neutrons (MeV). The proposed materials test station (MTS) at the LANSCE neutron facility at Los Alamos National Laboratory, will produce neutrons in the fast spectrum, but will again only be able to produce approximately 20dpa of damage per year. It should be noted that even fast neutron reactors typically take several years of exposure to produce damage levels of 150-200dpa.

Table 1. A comparison of characteristics of various neutron generating test facilities

Facility (# of irradiation positions)	Fast Flux ($n/cm^2/s$) E>0.1 MeV	Neutron Damage (dpa)	Linear Power (W/cm)	Fast to thermal ratio	Burnup	Volume (diam x length)	He/dpa in ferritic steel
GNEP	2.0E15	150-200	300-350	>100	20-30%	6 x 60 cm	0.2-0.3
ATR (A holes - 16)	3.7-5.0E14	6-10/yr	300-350	1-1.2	No limit	1.6 x 120 cm	0.2-0.3
ATR (H holes -14)	3.7E14	6-10/yr	300-350	0.9	No limit	1.6 x 120 cm	0.2-0.3
ATR (EFT)	2.1E14	6-8/yr	300-350	0.25-10	No limit	7.6 x 120 cm	0.2-0.3
HFIR (Target position 37)	1.1E15	18/yr	300-350	0.5	No limit	1.6 x 50 cm	0.2-0.3
HFIR (RB* position 8)	5.3E14	5-7/yr	300-350	25	No limit	4.3 x 50 cm	0.2-0.3
MTS (36 for fuels; 18 for materials)	1.3E15	18/yr	~ 360	>100	No limit	~1 x 12 cm	5-25

2. RAPID DISPLACEMENT DAMAGE THROUGH HIGH TEMPERAUTRE ION IRRADIATION

Ion irradiation has the ability and has been used to create much higher rates of irradiation damage as a means for accelerated testing of materials. The rate of damage using ion irradiation is controlled primarily by the atomic number of the ion used and the current of the ion beam. (Figure 2). Ion irradiation has been used to simulate irradiation damage in oxides and metals for use in nuclear waste, thermal reactors[1, 2], fast reactor[3], and nuclear fusion applications[4-6].

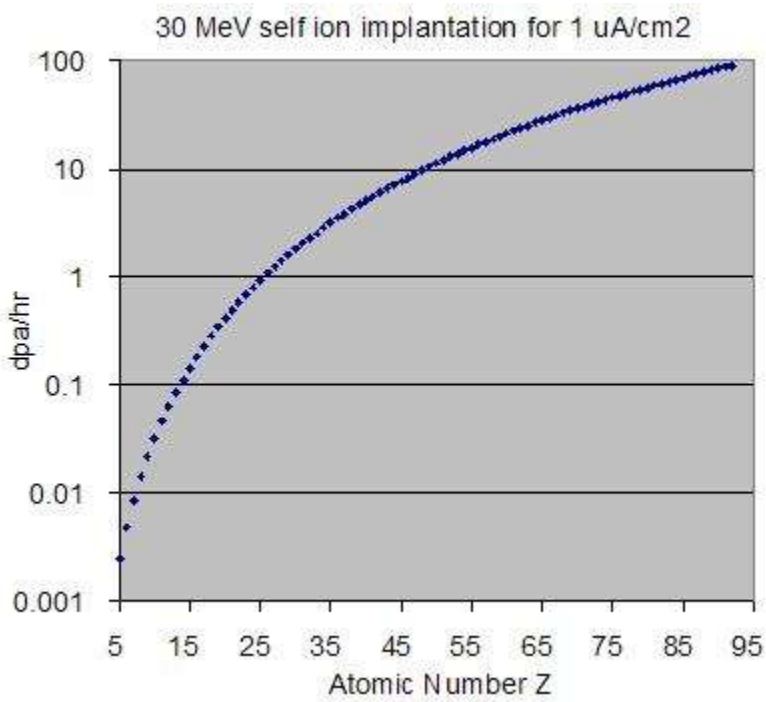

Figure 2. Ion damage simulation demonstrating the effect of the atomic number of the ion upon the damage rate at nominally room temperature.

Unfortunately, the damage profile resulting from ion implantation is limited in both spatial resolutions by the beam optics and in depth by the beam energy and atomic mass of the ion species and the specimen. This can be seen in the simulation of Frenkel pairs as a function of depth. This plot was based on the theoretical implantation of 30 MeV Fe into stainless steel into 1 square centimeter region for one hour at a current of one microampere. As can be seen, the majority of the damage exists at the end of range of the ions. This is known to result in a wide distribution in type and densities of defects found in the material as a function of depth. A schematic of the potential defects and the associated distribution can be seen in Figure 3. The defects often include small dense dislocation clusters, dislocation loops of various sizes, large disordered dislocation structures, voids and bubbles of various sizes and even region denude of any defects. The resulting heterogeneous defect structure produced by ion irradiation makes the characterization of the microstructure and mechanical properties of the radiation damage produced by ion irradiation significantly more challenging than that produced by neutron or gamma radiation exposure.

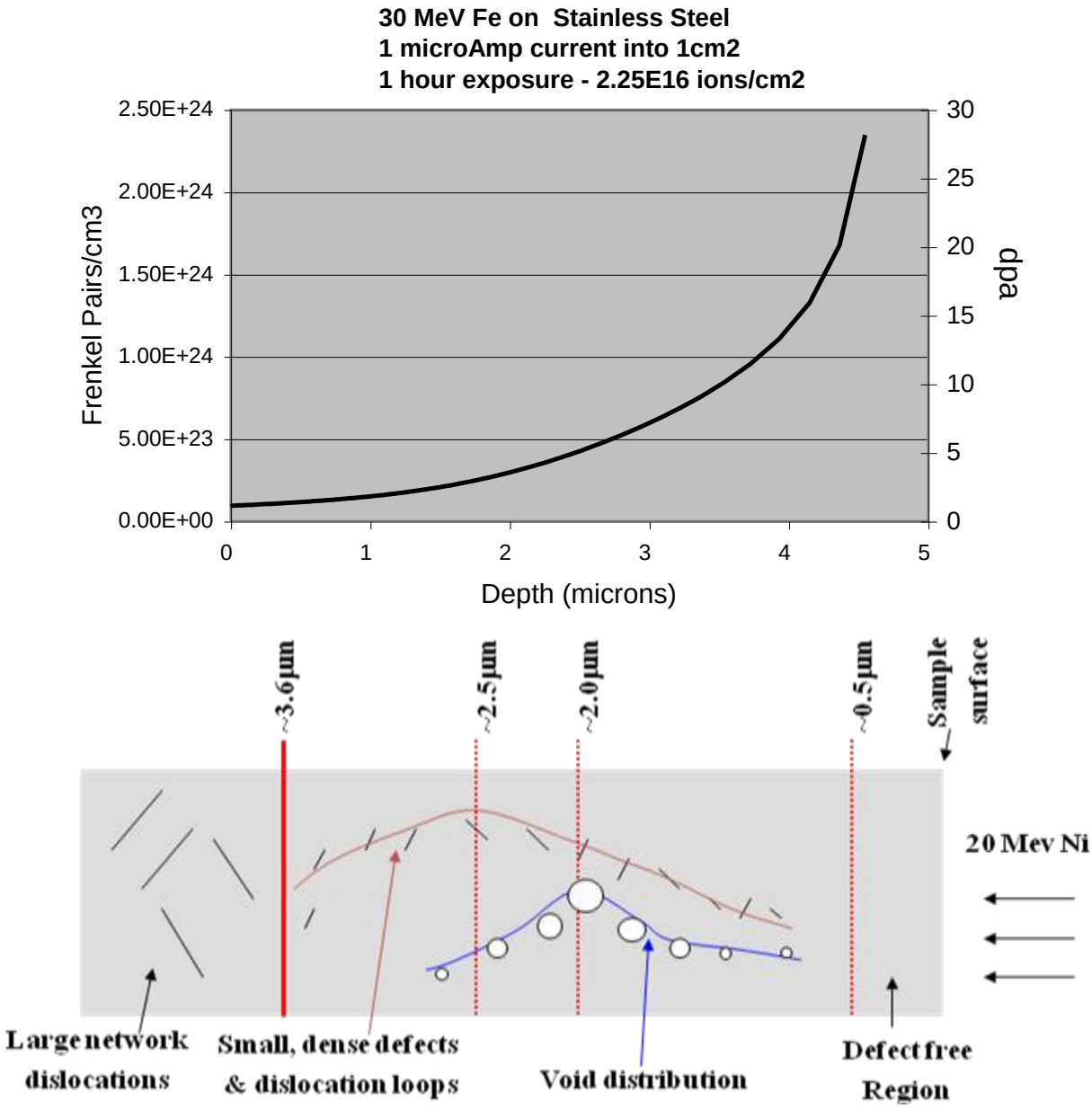

Figure 3. A plot of the irradiation damage as a function of depth in stainless steel and a schematic of the various defect structures that might result from ion implantation

To obtain a fundamental understanding of irradiation effects in core reactor materials required for modeling and advanced material development, we are developing an accelerated test bed which combines high energy (MeV) ion irradiation with *in situ* microscopies and mechanical testing capabilities to characterize the microstructural evolution and mechanical behavior of materials as a function of stress, temperature, and irradiation damage level. This report summarizes our initial work to bring these heavy ion beam capabilities on line. Specifically, we will discuss the instrument modifications made to allow control of the sample temperature and the measurement of the ion current. We will also describe work to generate three different kinds of transition

metal ion beams and the initial use of these beams to perform implantation experiments on steels specimens.

It is a great technical challenge to match the damage produced by years of fast neutron exposure with that damage produced by hours of heavy ions. Two of the most important variables for trying to match the damage are the sample temperature and the ion current of the beam. While the Ion Beam Laboratory at Sandia National Laboratories has previously performed *in situ* heating experiments and routinely measures ion beam currents, the simultaneous control of these two parameters required some specific instrumentation. Based on literature experiments, we need to be able to irradiate the samples at temperatures up to 600˚C.[3] We are using commercially available button heaters to heat samples approximately 8mm on a side up to these temperatures (Figures 4 and 5). As Figure 5, shows, there are some improvements that need to be made with the temperature control. The ion beam itself actually heats the sample to at least 100˚C (at ion beam current of 500nA) without any power applied to the heater. In addition, the 600˚C experiment seemed to have excess thermal expansion of the steel sample that may have created contact problems between the heater and the specimen.

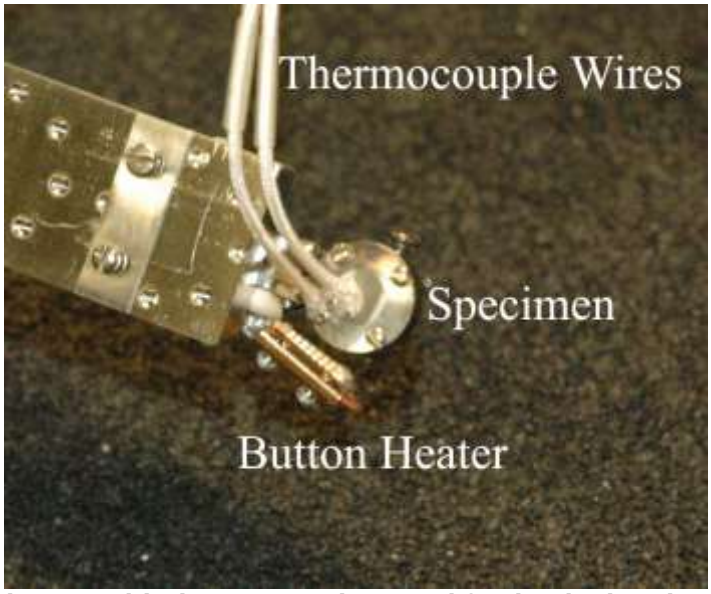

Figure 4. Button heater with thermocouples used for *in situ* heating experiments.

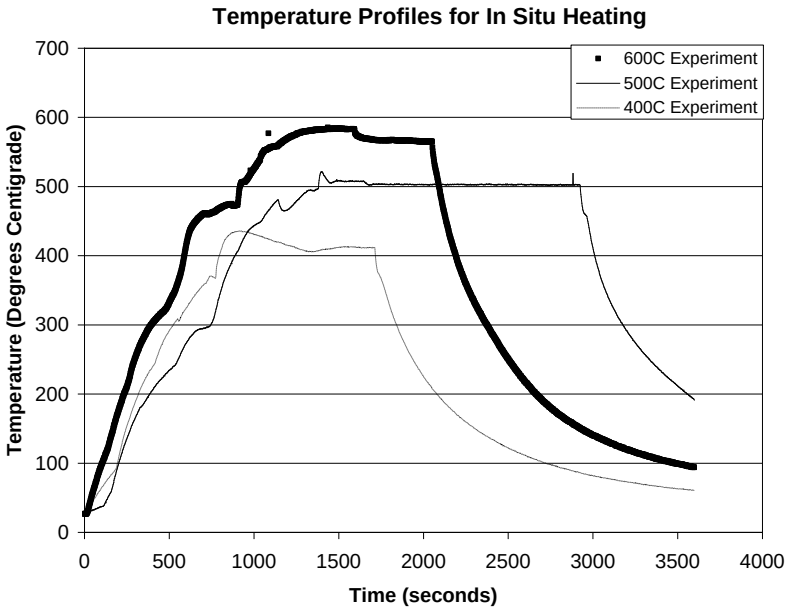

Figure 5. Control of temperature for *in situ* heating during ion implantation

Typically, ion beam currents can be measured by electrically isolating the specimen from the rest of the ion chamber and then measuring the ion beam current directly from the specimen. However, at the elevated temperatures required, there is a high enough leakage current develops which will not allow this method to be used. Instead, we have employed the use of a beam chopper up-stream of the sample to measure the ion beam current at these temperatures. The beam chopper was calibrated to the direct sample current measurement at room temperature, with a signal level ratio of approximately 1:5.

3. PROOF OF CONCEPT

To prove that this concept of using heavy ions combined with small scale mechanical testing initial test were done to determine the extent of damage structural materials using heavy ions.

3.1. High-Energy Heavy-Ion Irradiation Conditions

As noted above, the use of heavy ions (Z>20) is necessary to achieve the damage rates necessary for reaching damage levels of 150-200dpa in a reasonable amount of experimental time (approximately 1 day). In addition, it is also advisable to do self-ion implantation whenever possible. When possible, an ion beam should be chosen which alters the composition of the material being studied as little as possible. True fast neutron exposure can actually alter the composition of the material somewhat by the process of transmutation (e.g. production of helium).

For cladding steels, the base element is iron (Z=26). The use of an iron ion beam would be ideal to avoid altering the material composition. Unfortunately, it can be difficult to produce an iron beam of sufficient intensity (at least 25 nA/mm^2) to reach the required damage rate. Two attempts were made to generate an iron beam. The first approach used a commercial, pure iron cathode from NEC. However, this experiment only resulted in an ion beam current of $3nA/mm^2$. The second approach uses hydrogen gas injected through a hole drilled through the metal cathode to form a metal hydride which can be ionized and accelerated. This approach is not yet working, but the ion source of the instrument was recently repaired which should improve the ion beam yields for both iron ion beam approaches.

We were able to generate a copper ion beam with high intensity (several hundred nA/mm^2) that will allow damage levels up to 200dpa. However, use of the copper beam will somewhat alter the composition of the steel in a way that does not well simulate the fast neutron experiment. An copper ion beam with 1μA of current implanting into a $1cm^2$ area of pure iron with a 5μm end-of-range with create an average mole fraction of $5*10^{-4}$ copper in the iron. While this is not a large value compared to most alloy additions in the steel, it could change the microstructural response and mechanical properties if the copper were to segregate to grain boundaries or form precipitates.

In the ion beam implantation literature, a fair amount of work has been done with nickel ion beams. [3, 7] Some steels of interest, e.g. 316 stainless, already have a large amount of nickel added to the alloy (10-14wt%), so the additional nickel ions from the ion beam will not meaningfully alter the material composition. After repairing the ion source assembly, we were able to generate nickel ion beams of up to $1\mu A/mm^2$ in current. This nickel ion beam was used to perform most of the implantation experiments described below.

The goals of the initial implantation experiments were to 1.) establish temperature and ion beam current control and 2.) generate defects (e.g dislocation loops and nanovoids) that can be matched to previous experiments in the literature. The ability to establish temperature and ion beam current control has been discussed above. For the second goal, we chose three basic, struc-

tural steels which represent the three main classes of steels of interest in cladding and structural applications in fast neutron reactors: austenitic, ferritic, and martensitic. The austenitic, stainless steel 316L was chosen for the initial implantation experiments because previous experimental data is available and can be used to judge our current experimental approach. The work of Sindelar et al. used 14MeV nickel ion beams to examine void formation in 316L steel.[8, 9] Based in part on this work, we performed our implantations at 400, 500, and 600˚C using a 20MeV nickel ion beam with a flux of (400-500nAcurrent/3mm2) The choice of the energy of the ion beam affects the current available for the implantation and the depth of the implantation. An implantation depth of 3-5μm is sufficient for our experiments. As can be seen from the SRIM simulation, the choice of 20MeV gives a sufficiently large ion current with a mean implantation depth of 3.6μm. These samples will be prepared for defect analysis using the transmission electron microscope (TEM) in the next fiscal year.

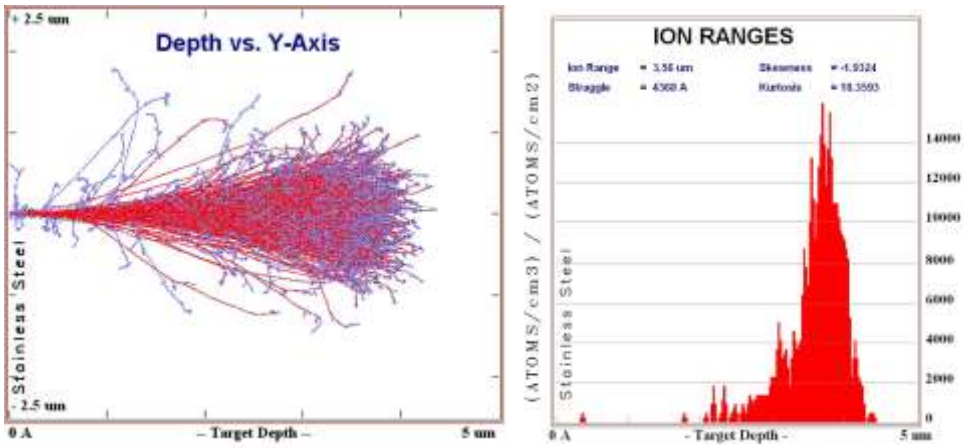

Figure 6. SRIM simulations of ion scattering of 20 MeV nickel into stainless steel. Note that the mean ion range from this simulation is 3.6μm.

We did perform initial TEM analysis of stainless steels implanted at nominally room temperature with 30MeV copper ions. We used a beam current of 100nA/mm^2 with a fluence sufficient for producing 15-20dpa at end of ion range. The experiments examined some of the basic ion damage characteristics and sample preparation issues for three stainless steels:

304 (austenitic, Fe, <0.08% C, 17.5-20% Cr, 8-11% Ni, <2% Mn, <1% Si, <0.045% P, <0.03% S),

420 (martensitic, Fe, <0.15% C, 12.0-14.0% Cr, <1.0% Mn, <1.0% Si, <0.04% P, >0.03% S),

e-brite (ferritic, Fe, <0.2% C, 25-27.5% Cr, 0.75-1.5%Mo,<0.2% Cu, <0.4% Mn, <0.4% Si, <0.02% P, <0.02% S)

The TEM samples were prepared by focused ion beam (FIB) cross-sectioning using a 30keV Ga ion beam. The TEM imaging STEM microanalysis work was performed using the Tecnai TF-30 300keV TEM/STEM with an EDAX energy dispersive x-ray detector. These samples did not show remarkable void or dislocation loop formation, probably because of the limited damage level in the experiment and the relatively low temperature of the implantation. There was

marked compositional mixing at the surface of the e-brite specimens. The compositional mixing was monitored by calculating the Cr/Fe ratio as a function of distance. This ratio should be constant for an un-irradiated steel. The fact that the Cr/Fe trace for the pristine 304 stainless steel specimen shows the same increase for the top 30nm as observed in the damaged areas for 304 and 420 stells, suggests that this is some sort of artifact and that there was little compositional mixing for the 304 and 420 stainless steels. The compositional mixing in the e-brite steel was also evident from backscattered electron SEM images (Figure 7). A clear phase separation was observed with a length scale ranging from 200-500nm.

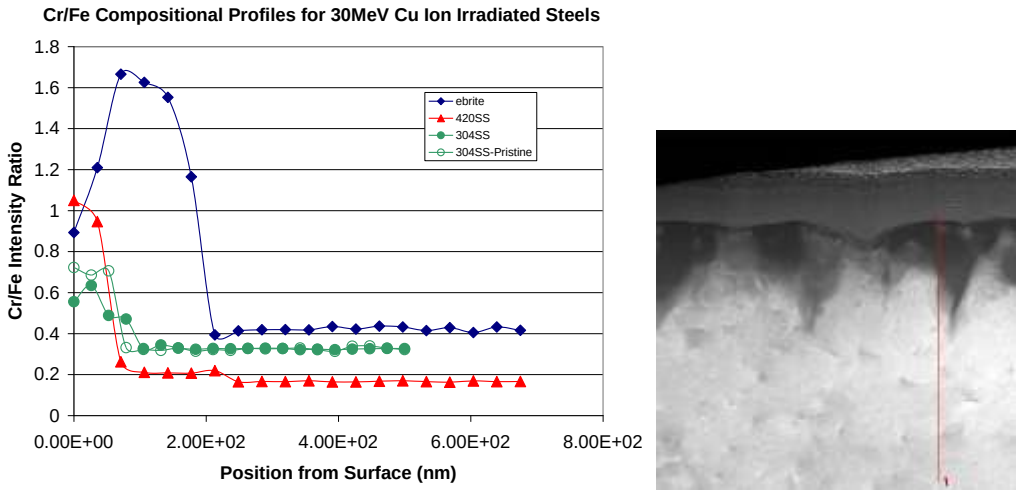

Figure 7. Compositional traces from STEM-EDX line profiles across copper implanted and pristine steel surfaces. A.) compositional traces, B.) annular dark field image from e-brite steel.

A.) Surface of pristine steel B.) Surface of irradiated steel

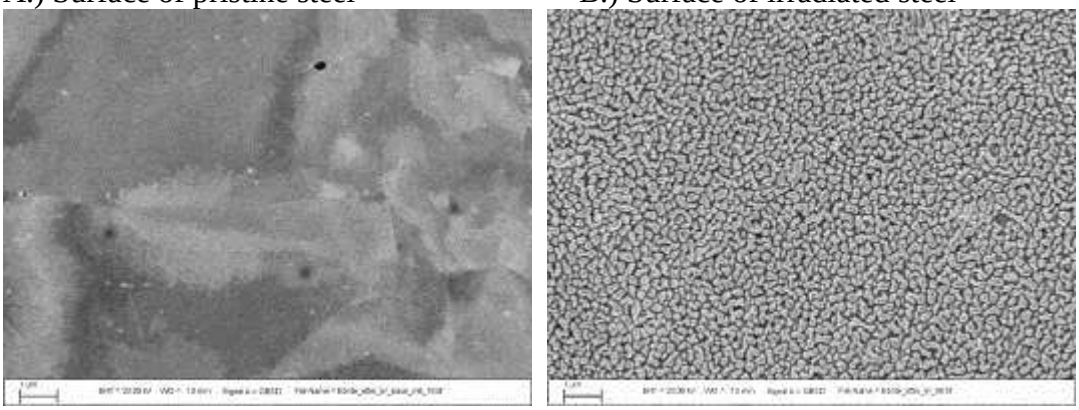

Figure 8. SEM micrographs of pristine and irradiated ebrite steel (Fe-26Cr-1Mo) using a 30MeV copper ion beam at room temperature. (experiment performed at SNL) Note the pronounced phase separation in these backscattered electron images.

3.2. Micropillar Compression Production

Single crystal high purity copper samples of <001>, <011>, and <111> orientations were obtained. 30 MeV Cu ions were used to irradiate a region of a millimeter squared in the center of the sample. By during self-ion implantation, the composition of the sample remained unchanged, while the microstructure of the sample was exposed to approximately 100 dpa. Focused ion beam (FIB) milling was then used to produce an array of nine micropillars in the local region to provide greater statistical certainty of the results. An example of an array milled into the single crystal Cu can be seen in Figure 9. These were the first micropillars produced at Sandia adding a new capability to do small scale mechanical testing not previously available. The pillars were milled using the technique developed by Dr. M. Uchic or a modification there of. [10, 11] As such, all of the pillars have a ratio of 2:1 between the height of the pillar and the diameter of the pillar. These dimensions and milling parameters have been optimized to minimize bucking and provide the most direct insight into the pillars mechanical properties when compressed using a flat head punch on a nanoindentation tool.

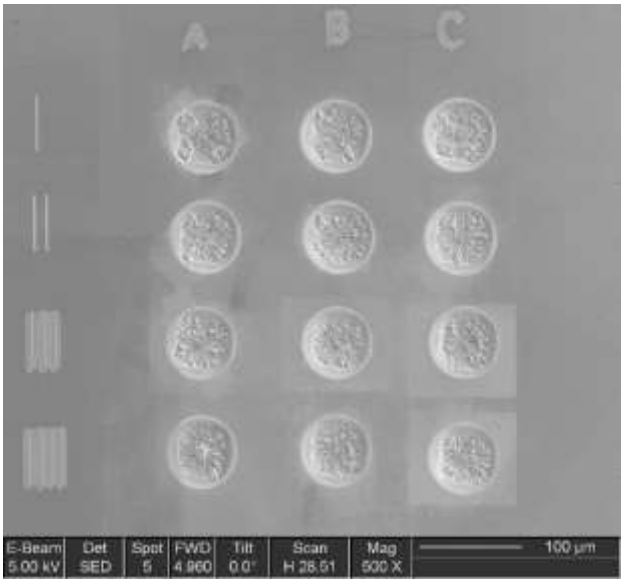

Figure 9. An array of micropillars created in single crystal Cu by FIB

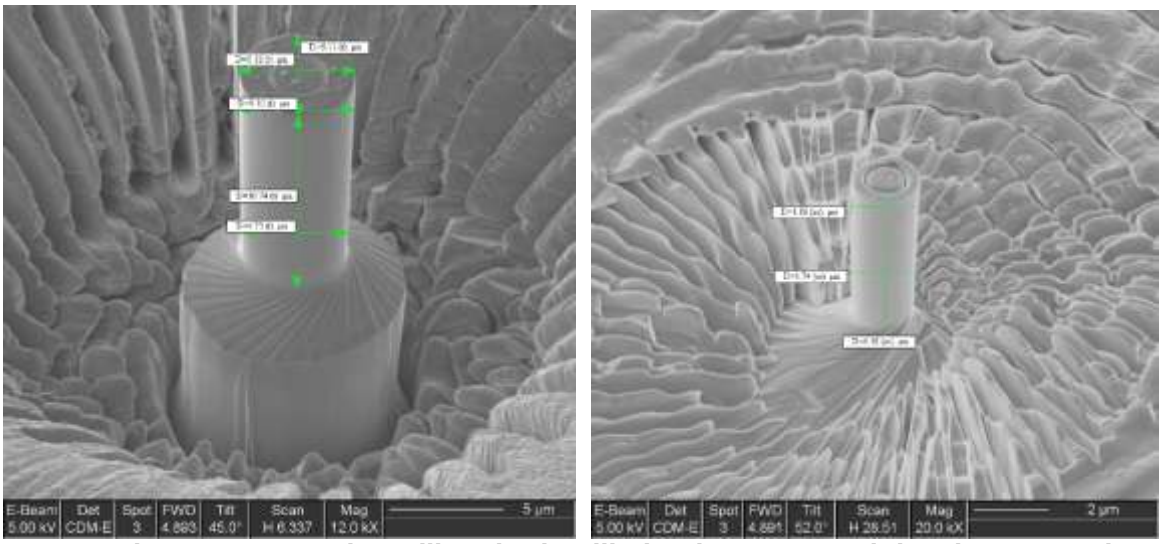

Figure 10 Two micropillars both milled to have 2:1::Height:Diameter ratio.

The first set of pillars produced at Sandia from each single crystal Cu orientation was made to the standard dimensions of 10 µm tall and 5 µm in diameter can be seen in Figure 10. This was done using the recently standardized dimensions in the micropillar field. As later results will show, this standard proved inadequate for the evaluation of self-ion irradiation damage and as such smaller micropillars were produced. This was done by scaling down the micropillar dimensions in the milling using the Uchic protocol. This resulted in pillars as small as the second image in Figure 10. This pillar has dimensions of approximately 4 µm tall and 2 µm in diameter. In total an array of pillars were produced for both the irradiated region and a control region at three different sizes resulting in a total of 81 miropillars produced in the single crystal Cu samples.

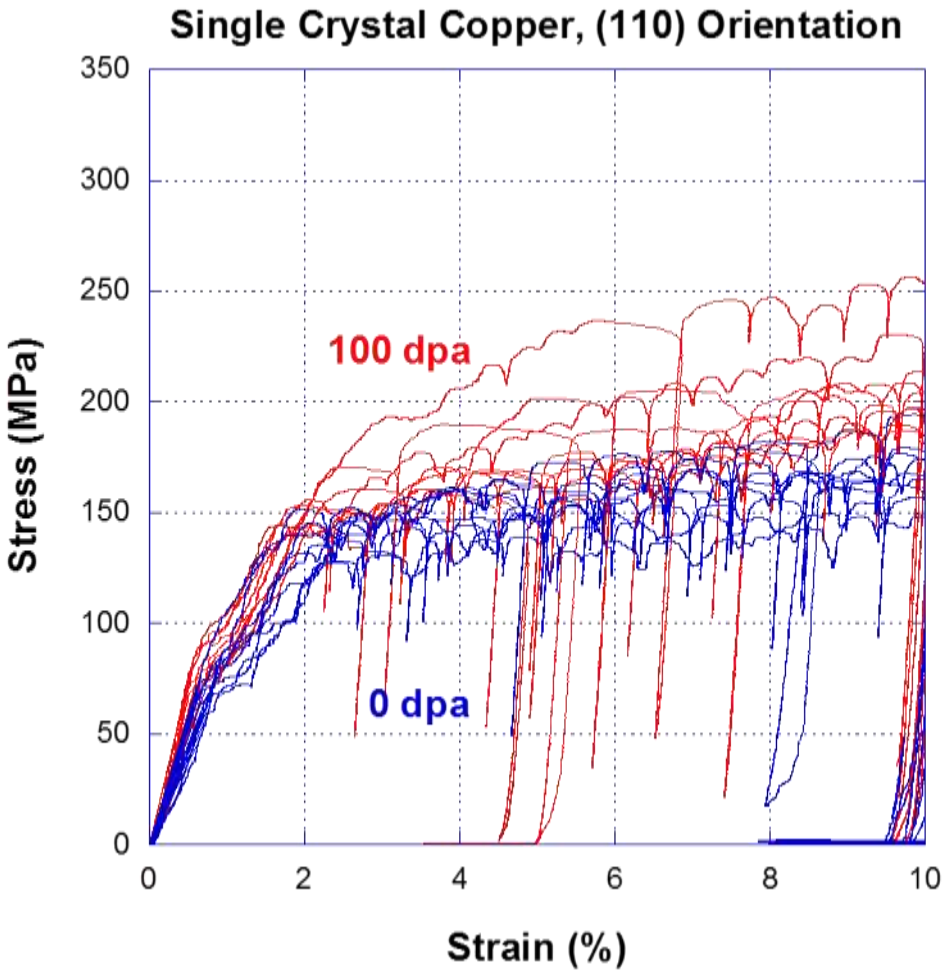

Figure 11. Stress strain curves from the control and irradiated 10 µm tall pillars

Figure 11 is a stress-strain curve resulting from the compression of the first 18 micropillars produced. In blue is the control pillars that had not been exposed to self-ion implantation and in red is the samples that had been exposed to approximately 100 dpa worth of damage. Contrary to what was expected, the difference in the data sets is within the scatter within each data set. This without further explanation would suggest that minimal mechanical property damage in observed in ion irradiated single crystal Cu even up to damage levels as high as 100 dpa.

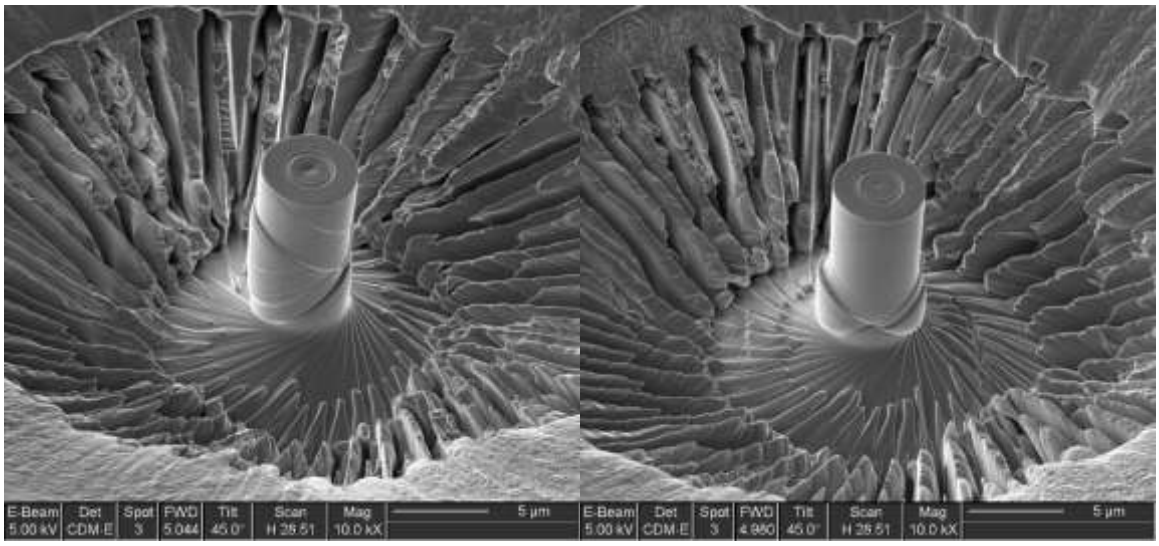

Figure 12. Deformed pillars after compression of the irradiated and controlled 10 µm tall pillars

However the discrepancy between the prediction and the data presented in Figure 11 was quickly solved when the micrographs of pillars were taken. As can be seen in Figure 12, the control pillar on the left contains slip band running the entire length of the pillar. Whereas, the irradiated pillar on the right has slip bands that only propagate on the bottom half of the pillar. These slip bands are at height lower than the end of range of the copper ions and are this in virgin material that is expected to react similar to that of the controlled sample. To avoid the effect of the ion implantation length scale on the recorded micropillar mechanical response, smaller pillars were produced using modifications to the same milling protocol.

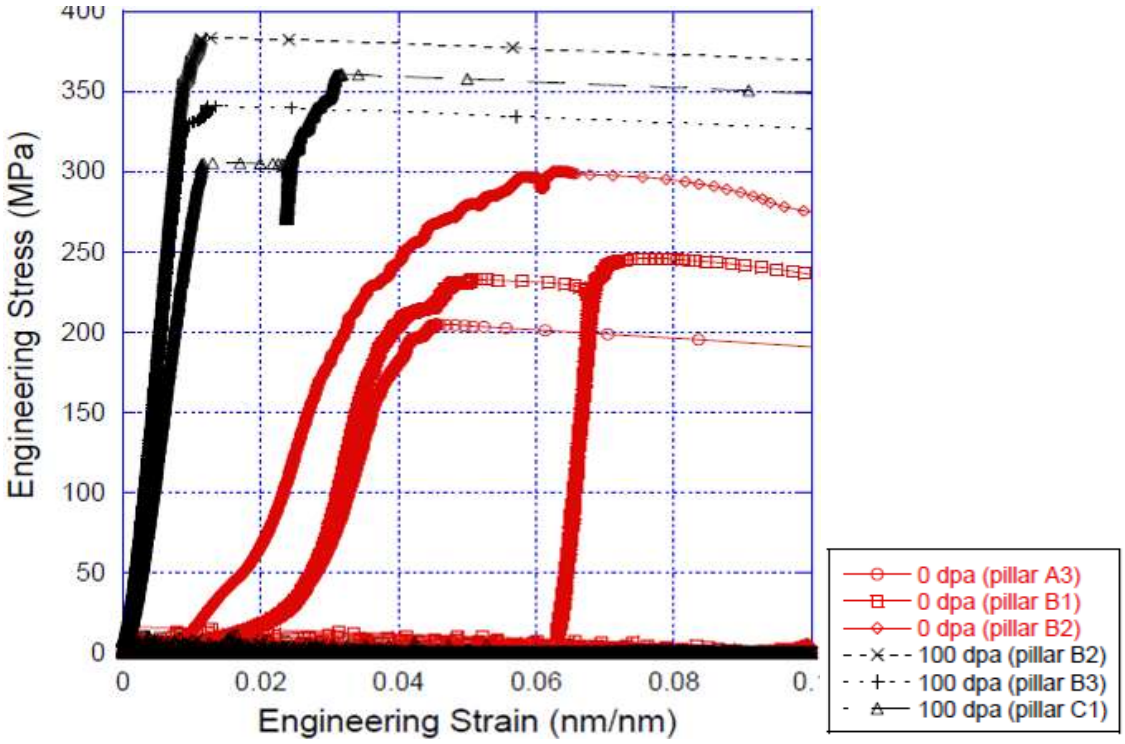

Figure 13. Stress strain curves from the control and irradiated 5 µm tall pillars

The pillars produced to be 5 µ tall and 2.5 µm diameters were produced and compressed using identical FIB and nanoindentation facilities. In contrast to the taller pillars a distinct difference in the strength of the pillar in compression can be seen with the irradiated pillars being approximately 100 MPa stronger. In addition, the irradiated micropillars appear to fail significantly less total strain. These are the expected decease in ductility and increase in strength associated with irradiation damage due to the accumulation of defect clusters, such as dislocation loops that prevent the natural slip of glide dislocations.

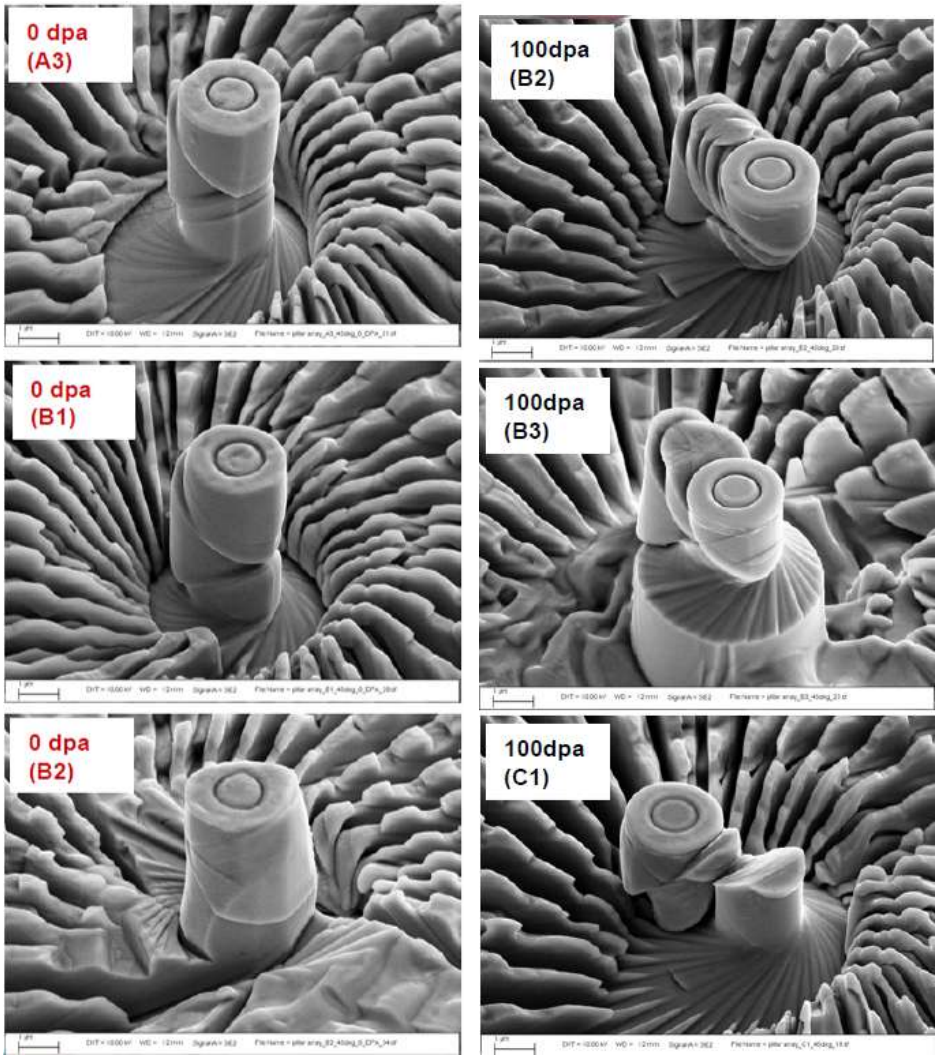

Figure 14. Deformed pillars after compression of the irradiated and controlled ? µm tall pillars.

The failure of these ion irradiated pillars was catastrophic in nature and resulted in significant deformation of the pillar. This can be seen in the images on the right of Figure 14. In most of these pillars the greatest slip occurred at the base (B2 and B3) or in a region approximately a micrometer above the base (C1) of the pillar. The slip at the base might be explained as a small sec-

tion of the pillar is in the virgin copper crystal and can thus easily slip relative to the rest of the pillar, although not through a complete slip plane as was seen in the taller pillars. The sample that slip occurred about one micrometer above the base might be a result of the heterogeneous nature of heavy ion irradiation. The end of range of the implants produces the greatest amount of damage and would be hypothesized to be the strongest portion of the pillar. In order t investigate the effect of end of range on the resulting stress-strain curves, even smaller pillars were produced.

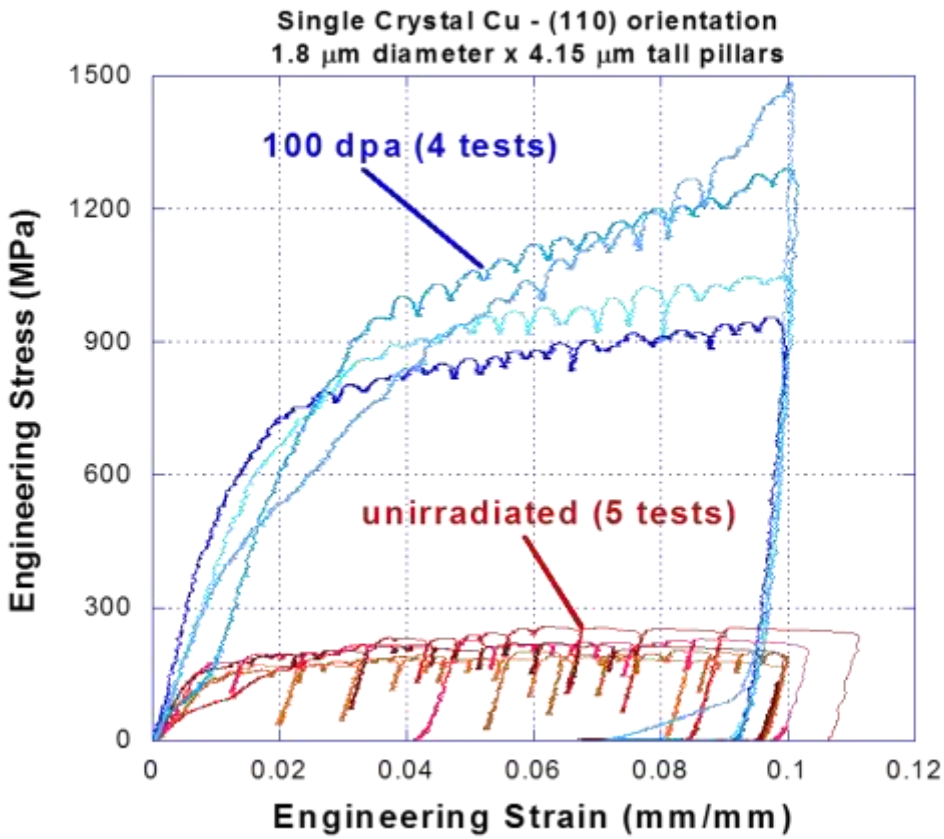

Figure 15. Stress strain curves from the control and irradiated 4 μm tall pillars

Figure 15 is the stress-strain curve micropillars designed to be 4 μ tall and 2 μm diameters. It should be noted that as the pillars get smaller the tolerance of the process remains the same, which should increase the scatter in the data. Despite this effect, the greatest separation between the control and ion irradiated data can be seen in this data set. The virgin copper pillars should typical copper response with a maximum strength in compression around 200 MPa and an elongation, which is similar to that seen in all of the controlled experiments independent of height. In contrast, the irradiated pillars demonstrated compression strengths as high as 1500 MPa. This is nearly an order of magnitude higher than the control samples and over three times that of the 5 μ tall and 2.5 μm diameters pillars. This suggests that the inclusion of the end of range of the ions in the pillars plays a significant role in the deformation and failure of the pillars.

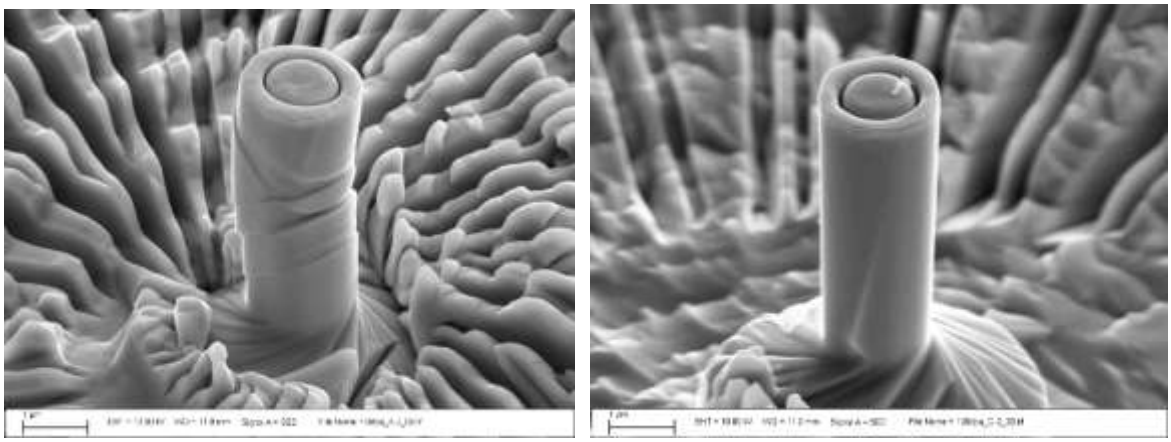

Figure 16. Deformed pillars after compression of the irradiated and controlled 4 µm tall pillars.

SEM images of the controlled and irradiated be 4 µ tall and 2 µm diameters pillars after compression can be seen in Figure 16. As expected, the controlled pillars exhibit slip bans throughout the pillar height running along the 111 family of slip planes. In contrast, the irradiated pillar shows no signs of slip in the pillar dimension, as is evident by the milling defect still present in the pillar shown. This lack of deformation is in agreement with the increased hardness of the pillar observed in the stress-strain curve.

The results of these sets of experiments show that micropillar compression provides significant amount of information that can be used to characterize the effects of ion irradiation, but are limited in applicable conditions. The volume of the pillar must be larger enough to encompass any inhomogeneity in the material investigated and small enough to contain only the relatively flat part of the irradiation damage profile.

3.3. Individual Micropillar Irradiation

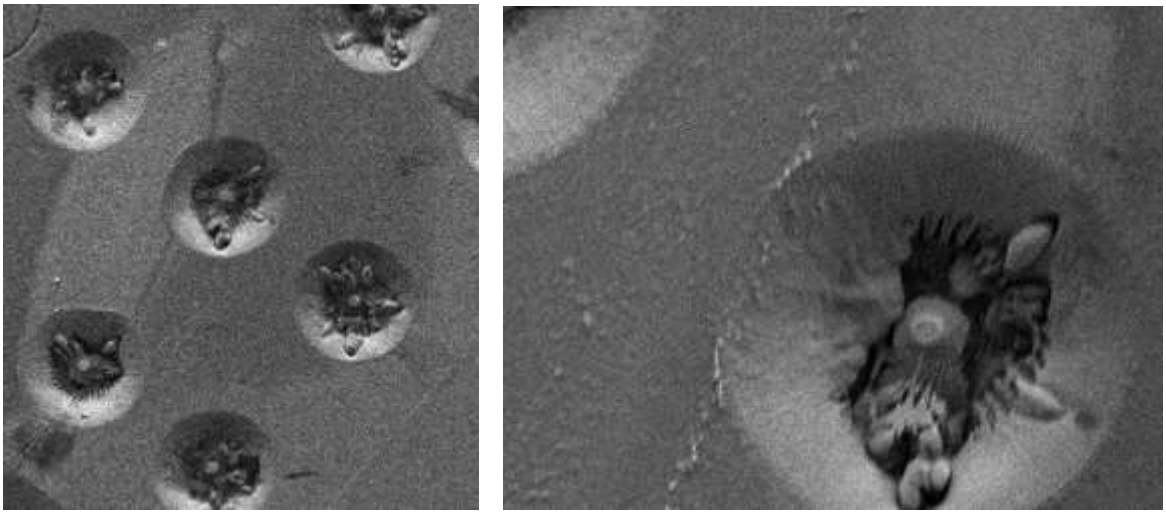

Figure 17. SEM images of irradiation damage of select pillars in within an array

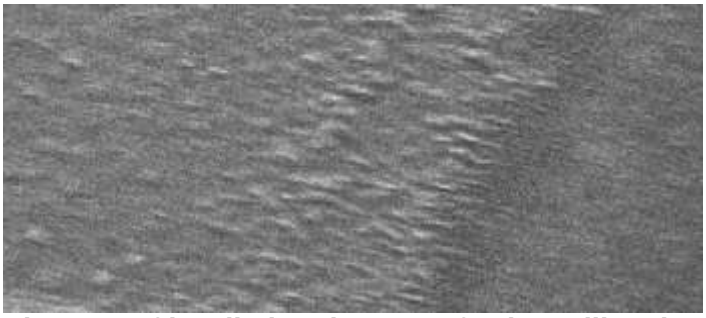

Figure 18. SEM images of irradiation damage of select pillars in within an array

In addition to the effort detailed to produce pillars after ion irradiation of a sample, a project was undertaken to irradiate the pillars after milling. The large control pillars produced in Figure 10 that were be 10 µ tall and 5 µm in diameters were irradiated using an in-situ optical microscope to align the ion beam with the pillars during irradiation. The results of this effort can be seen in Figure 17. The radiation damage could be observed using the nearly in-situ ion irradiation SEM during the implantation. It was determined that the geometrical tilting and rotating requirements required to provide uniform damage distribution in the pillar was extensive and thus not feasible. Pior to recent upgrades in the system the resolution of the SEM only permitted a general characterization of the radiation damage after extensive irradiation damage had been produced. This can be seen in the blistered region of Figure 18.

4. QUALIFICATION OF TECHNIQUE IN STAINLESS STEEL

4.1. Finite Element Modeling of Nanoindentation into Irradiated Steels

To determine if the effects of irradiation damage would be detectable by nanoindentation, an axisymmetric finite element model was created to simulate the nanoindention experiment using a conical tip with an effective cone half-angle (19.7º) of a sharp 3-sided diamond Berkovich tip. [12, 13] The finite element mesh of the model is shown in figure 1. The size of the substrate in this simulation is a 60 µm by 40 µm and contains a sub-surface hardened region, highlighted in red,. The bottom of the substrate is fixed in the simulation and the hardened region is 2.5 um thick situated between 2.5 and 5 um beneath the substrate surface. It is included to capture the effect of a radiation hardened layer beneath the surface of a 300 series stainless steel sample. In the simulation, the diamond indenter has a Young's modulus of 1141 GPa and a Poison's ratio of 0.07. The substrate has a Young's modulus of 200 GPa and a Poison's ratio of 0.3. The coefficient of friction between the tip and the surface was set as 0.1. The yield strength of the substrate, , was set to 350 MPa. To provide a first order approximation of a radiation hardened region produced by ion irradiation, the region outlined in red was set to yield strength of 700 MPa.

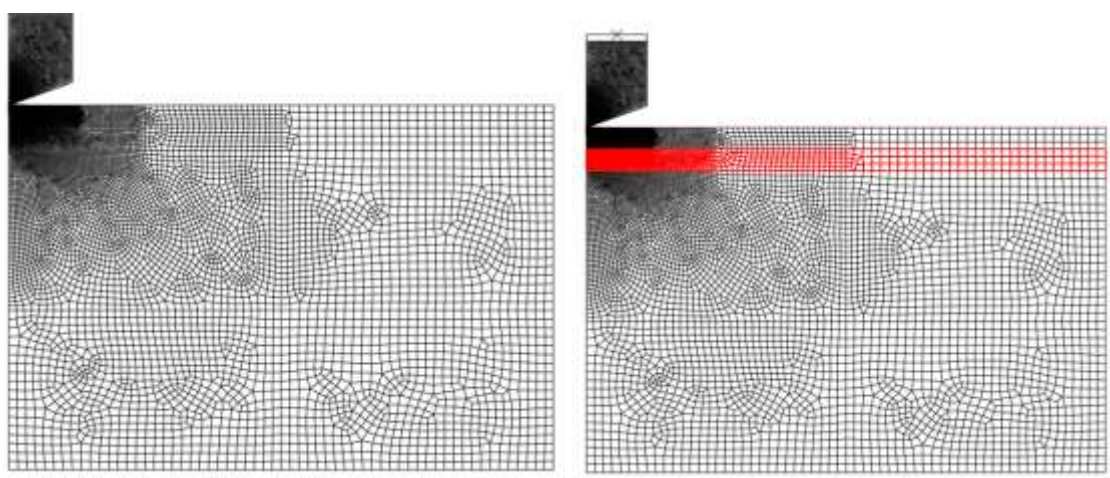

Figure 19.Finite Element Model of conical indentation of a control and a irradiation hardened microstructure

A simulated result demonstrating the effect of the subsurface hardened layer is given in Figure 20. It is a plot of hardness, i.e. load divided by projected contact area, vs. indentation depth. For comparison, the same result from simulation without a hardened region is also plotted in Figure 20. The comparison shows the increasing influence of the hardened region as the indentation depth increases, even though the maximum depth in the simulation is significantly less than the depth of the hardened region. This result suggests that the plastic zone ahead of the indentation tip begins interacting with the hardened region, at an indentation depth of about 500 nm deep. The hardness was found to increase as with increasing indentation depth suggesting that nanoindentation should provide an adequate technique to sample the radiation damage in the limited volume that is produced by ion irradiation.

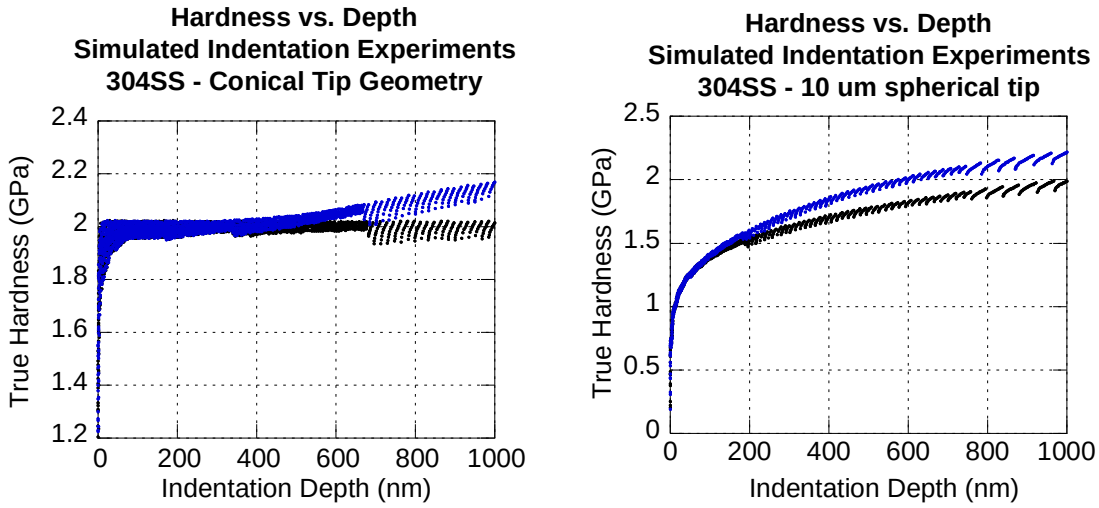

Figure 20. Simulated Hardness for both conical and spherical nanoindenters based on FEM simulation

4.2. Sample Preparation Ion Irradiation Conditions

All of the studies discussed in this section are based on nine 8 mm x 8 mm sample coupons that were cut and mechanically polished to a mirror finish from the same stock of steel. All of the 316L was cut from the same sheet of 316L AK Steel. The manufacture reports the tensile strength as 631 MPa the 0.2% offset yield strength as 331 MPa, and the Rockwell hardness as 82. The coupons were grinded and polished culminating with a final polish of the coupons using a vibratory polish and colloidal silica. Similarly, all of the 420F steel discussed in this section were produced from the same 12.7 cm diameter rod manufactured by Bralco Metals. The rood was cut into 8 mm x 8 mm sample coupons and polished to a mirror finish using a final vibratory polishing step. This sample preparation provided the mirror finished needed for both nanoindentation and various types of surface analysis in coupons suitable for the button heater seen in Figure 4.

4.3. Spherical Nanoindentation Results

Spherical indentations were investigated as a possible method to characterize the hardness of the material. Although not as standard as Berkovich indentation for nanoindentation, spherical indentation is in use and if done at elevated temperatures is able to provide some information on the creep behavior of the sample as a function of stress and temperature. [14, 15] Due to the importance of creep during the lifetime of the nuclear reactor under both high temperature and high radiation flux, a technique like that outlined in Figure 21 was considered using spherical indentation.

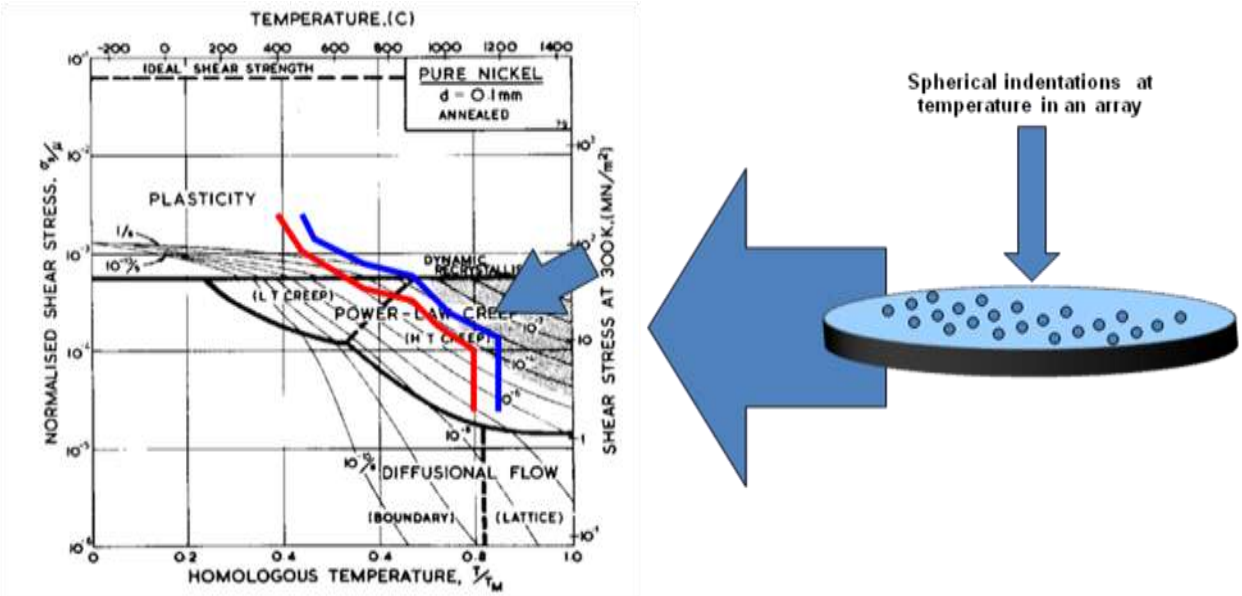

Figure 21. Schematic indicating the advantages of spherical indentation to provide information on the active creep mechanism

Spherical indentations of 316 L stainless steel irradiated to approximately 100 dpa at 400 ºC, 500ºC, and 600ºC can be seen in Figure 22. The results show a similar trends and values to that of the model created for the spherical indentation of 300 series stainless steel in the experiments ran at 400 ºC and 500ºC. The major deviation between the models is that the implanted region shows significant deviation from the perfectly elastic region of the hardness versus depth graph. This deviation might be a result of increase surface roughness in the irradiated material. The poor model fit for the 600ºC irradiated sample suggests that a microstructural evolution has occurred in the materials softening the irradiated region to be similar to that of the control sample.

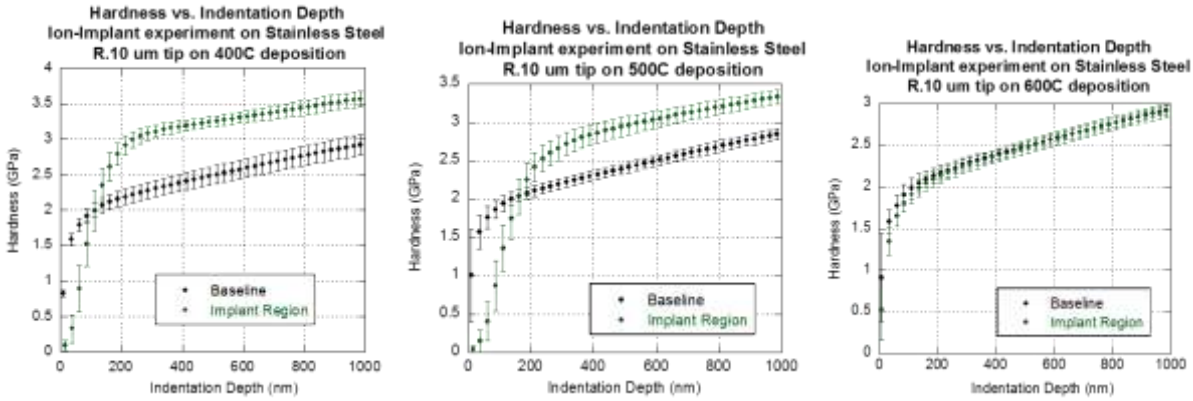

Figure 22. Hardness as a function of depth for spherical indentations at 400 ºC, 500ºC, and 600ºC

4.4. Berkovich Nanoindentation Results

In addition to the spherical indentation, Berkovich indentation was done to provide mechanical property information on the samples. This technique does not provide information related to the creep properties of the sample, but does provide information regarding the hardness of the local region and insight into the strength and ductility of the material. Because of the size of these indents, an array of indents such as those seen in Figure 23 could be included within the irradiated region providing some statistics over a heterogeneous microstructure.

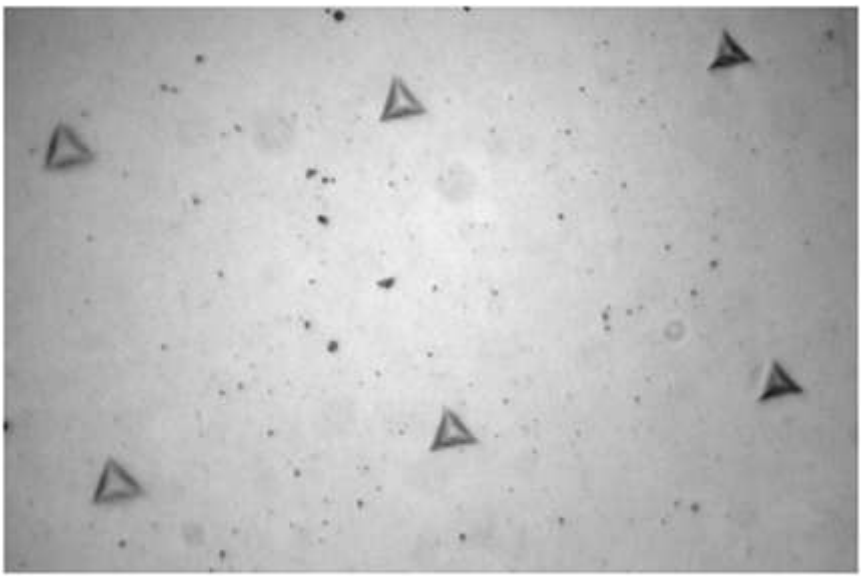

Figure 23. Optical Micrograph of an array of Berkovick indentations in steel

Table 2. The Matrix of indentation performed on 316L stainless steel

Experiment	Tests	H (GPa)	E (GPa)
400C baseline #1	16	2.46± 0.07	203 ± 10
400C baseline #2	16	2.40± 0.08	202 ± 7
400C implant region	16	3.07± 0.07	197± 7
500C baseline	14	2.30 ± 0.11	195 ± 6
500C implant region	15	3.05 ± 0.10	198 ± 11
600C baseline	16	2.33 ± 0.09	191 ± 8
600C implant region	16	2.36 ± 0.09	190 ± 9

As predicted by the finite element model, a distinction was observed in the majority of the ion irradiated regions when compared to the set of baseline nanoindentation results, as can be seen in Figures 24, 25, and 26. In the 316L coupon irradiated to approximately 10 dpa, the difference between the ion irradiated regions and the baseline was slight, falling within the error bars for the implants done at 500 ºC and 600 ºC. At approximately 40 dpa, a significant increase in hardness is observed between the baseline nanoindentation results and those of the 400 ºC and 500 ºC irradiation exposures. However, the hardness values for the material receiving a 40dpa exposure at 600 ºC remained similar to the baseline. This trend is enhanced in the 100 dpa set of implants resulting in a 1 GPa difference between the hardness of material ion implanted at 400 ºC and 500 ºC compared with the baseline and the 600 ºC implanted region.

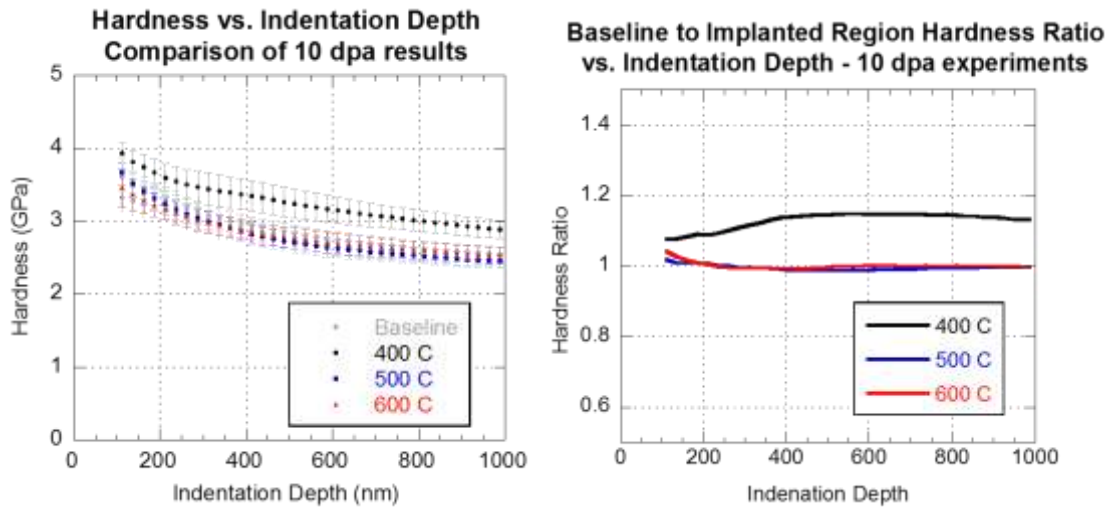

Figure 24. Nanoindentation results of controlled regions and irradiated regions to approximately 10 dpa at 400 ºC, 500ºC, and 600ºC

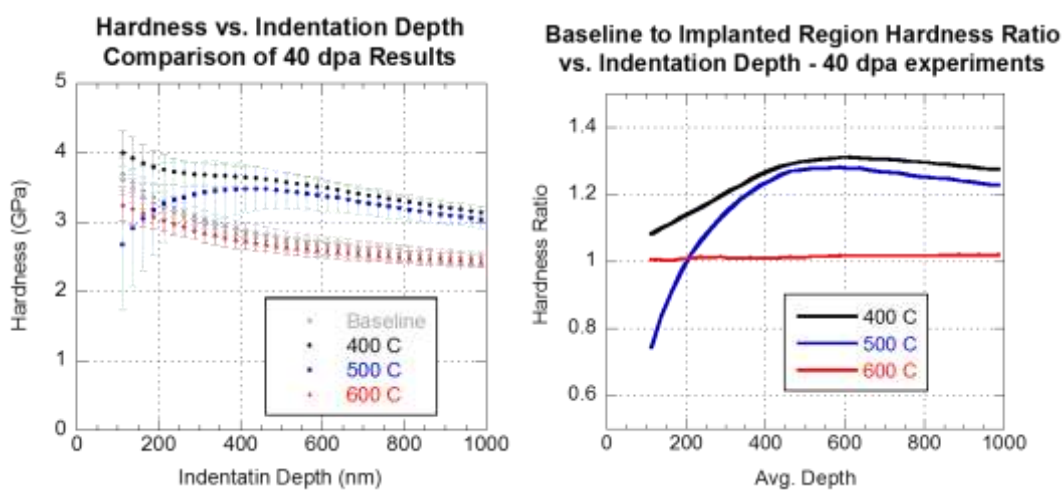

Figure 25. Nanoindentation results of controlled regions and irradiated regions to approximately 40 dpa at 400 ºC, 500ºC, and 600ºC

Initial analysis of the data raised a concern regarding the decreasing slope of the baseline hardness versus depth curves shown in Figures 24, 25, and 26. To determine if this was a small scale effect or if the surface had indeed been hardened during the metallographic sample preparation, the samples were electropolished. The electropolished baseline sample did not exhibit the same negative slope seen in the initial coupons suggesting that the negative slope seen was a result of work hardening that occurred in the relatively malleable 316L stainless steel. This work hardening appeared to be limited to the top 400 nm to 600 nm of the coupons and produced significantly less damage than the radiation damage produced in the majority of the coupons.

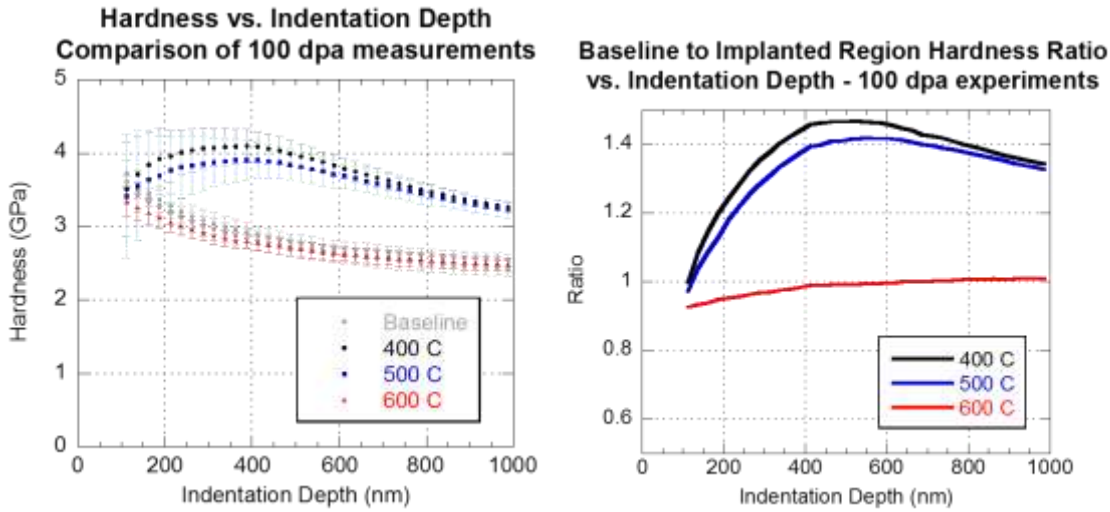

Figure 26. Nanoindentation results of controlled regions and irradiated regions to approximately 100 dpa at 400 ºC, 500ºC, and 600ºC

To distinguish between the radiation hardening from ion implantation and the work hardening from sample preparation, the data presented in Figure 1 is normalized to the baseline and is plotted again in the left side of Figures 24, 25, and 26 . The effect of increasing dose on the hardness ratio can be observed in both the 400 ºC and 500 ºC sets of coupons in the normalized data indicating that the effect of dose was significantly larger than the surface work hardening resulting from the vibratory polishing. Figure 4 also clearly demonstrates that there is minimal deviation between the baseline samples and the set of samples irradiated at 600 ºC. Because differences between surface and subsurface conditions can greatly affect nanoindentation results, it is strongly recommended that a baseline normalization and similar hardness ratio should be implemented in the rapid characterization of ion irradiation damage.

In addition to the experiments ran on the 316L stainless steels, a set of nanoindentations were done on 420F stainless steel. The 420F was polished and irradiated to similar condition of approximately 10 dpa, 40 dpa, and 100 dpa at temperatures of 400 ºC, 500ºC, and 600ºC. Table 3 outlines the number of test done for each irradiation condition, the hardness and elastic moduli of both the control and implanted samples. In comparing the data in the baseline column, a softening is evident as the temperature of the sample increases independent of the ion irradiation condition. In addition, a trend is observed as expected for increasing hardness with increasing radiation damage for samples irradiated at the same temperature.

Table 3. A set of nanoindentation experiments run on the 420 stainless steel

Sample	Temp.	# of Tests	Baseline (1um depth) H (GPa)	E (GPa)	# of Tests	Implant Region (1um depth) H (GPa)	E (GPa)
10/high	400	16	3.27±0.09	228±8	16	3.93±0.11	213±8
10/high	500	16	3.15±0.09	200±6	17	3.58± 0.09	229± 7
10/high	600	15	2.92±0.07	190±5	16	2.96±0.13	232±6
40/1	400	16	3.44±0.09	230±7	14	4.35±0.16	226±6
40/high	500	15	3.20±0.07	236±6	14	3.71±0.08	233±8
40/high	600	16	2.90±0.05	222±6	11	2.90±0.08	229±12
100/high	500	16	3.05±0.08	227±7	9	3.58±0.09	230±9

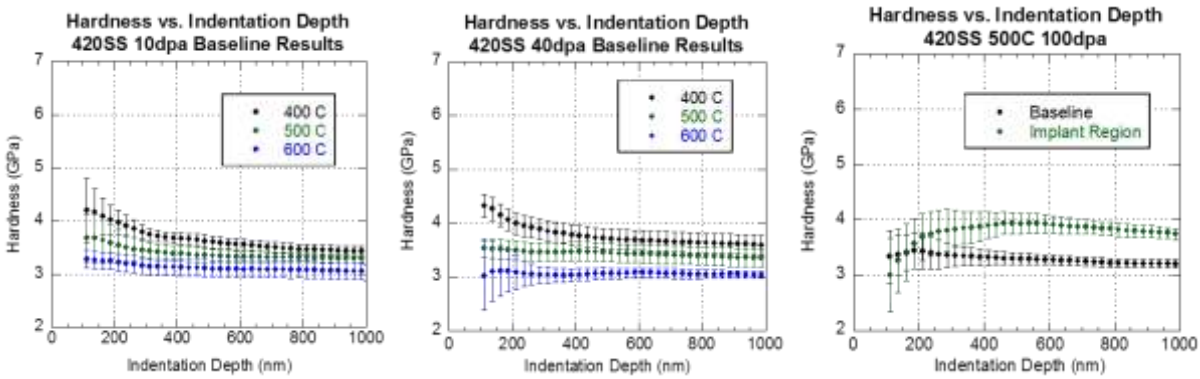

Figure 27. Nanoindentation results of controlled regions and irradiated regions to approximately 10 dpa, 40dpa, and 100 dpa at 400 ºC, 500ºC, and 600ºC

A plot of this data, Figure 27, permits one to better visualize the change in hardness as a function of depth into the materials. At the lowest damage level 10 dpa, there is no difference between the 600ºC and the control experiment and minimal difference between the 400 ºC and 500ºC sample and the control region. This separation increases at the approximately 40 dpa damage level between the 400 ºC, and 500ºC and the control sample, but is note present in the 600ºC sample and the control. This separation trend continues in the 100 dpa sample 500ºC sample. The downward trend in the implanted hardness near the surface was attributed to increase surface roughness due to the implantation, but might be an artifact of the denude zone present under these implantation conditions.

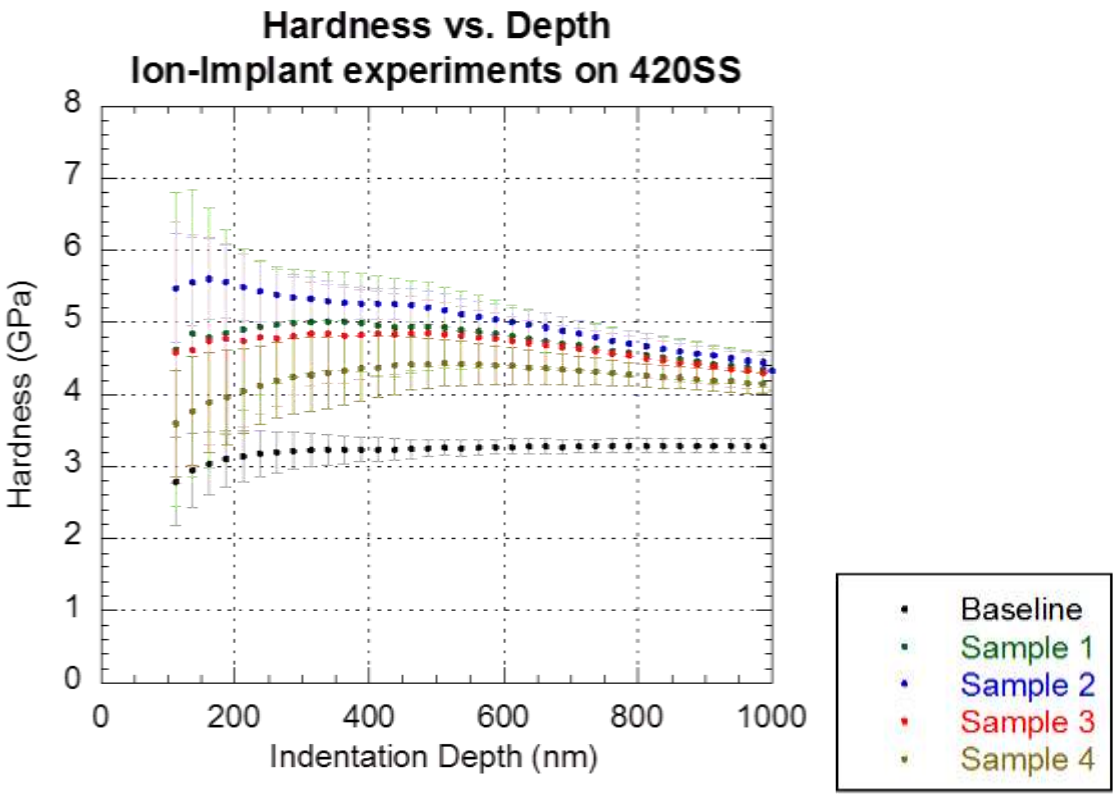

Figure 28. Nanoindentation results of controlled regions and irradiated regions. The samples were irradiated at various ion fluxes.

The 420F stainless steel was used for a experiment to investigate the effects of heavy ion irradiation rate on the resulting mechanical properties. Figure 28 is a hardness plot of the samples implanted at various rate. Sample 1 was implanted at the slowest rate possible, which resulted in extensive fluctuation of the ion beam. Sample 2 was implanted at half the implantation rate of the maximum implantation rate. Sample 3 was implanted at a quarter and sample 4 was implanted at an eighth of the maximum implantation rate. The results of this experiment is clear that the ion irradiation rate does alter the microstructure and subsequently the mechanical properties of the film and as such should be taken into consideration and at the minimum uniformed throughout all the implantation experiments performed. This deviation was not determined to be be either a direct result of the implantation rate or a secondary effect, as the sample was held at elevated temperatures for longer periods of time during the slower implantation rate in an effort to reach the same total dose.

4.5. Microstructural Examination of Irradiated Region

Due to the strong dependence between mechanical properties and microstructure in structural materials, an effort was made to quickly characterize the microstructure of the ion irradiated samples. The first effort that was made was the incorporation of an EBSD scan of this sample. If this could be done successfully, then a rapid nearly in-situ capability could be used for the characterization of the samples during ion irradiation. Figure 29 shows the EBSD maps obtained for both the control steel sample and the ion irradiated region of a 316L sample after 100 dpa at 600ºC. The EBSD map of the control samples provides significant insight into the texture of the

film and the type of grain boundaries present. In contrast, the region ion irradiated to a dose of 100 dpa showed minimal set of spots with adequate confidence index. This initial result suggests that EBSD maps will not be of great benefit for characterizing regions of heavy radiation damage.

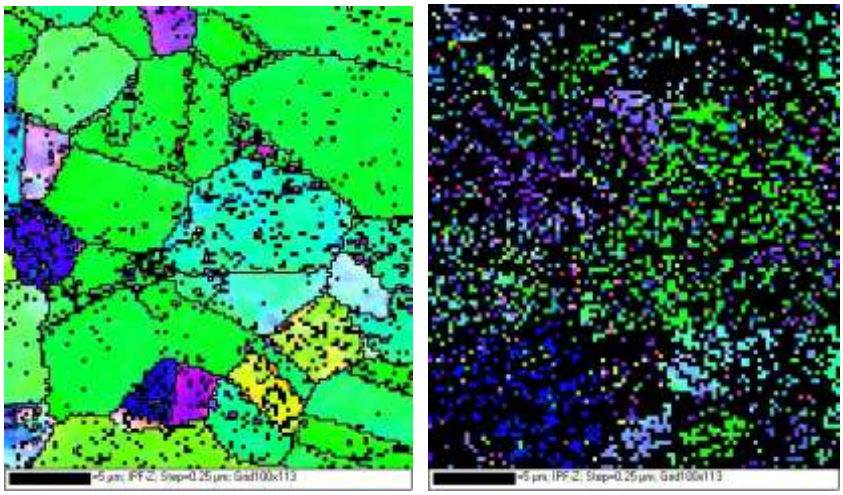

Figure 29. EBSD orientation map of 316L control and 100 dpa irradiated regions.

Despite the poor EBSD map, a pole figure can still be created with accurate data points for both the control and radiation damaged samples. This set of pole figures can be seen in Figure 30 for the same 316L stainless steel sample irradiated with 20 MeV Ni to approximately 100 dpa at 600ºC. It appears that at least under these conditions, the microstructure evolves from a 110 dominated texture to 111 texture. This effect provides some initial insight into the microstructural evolution that occurs.

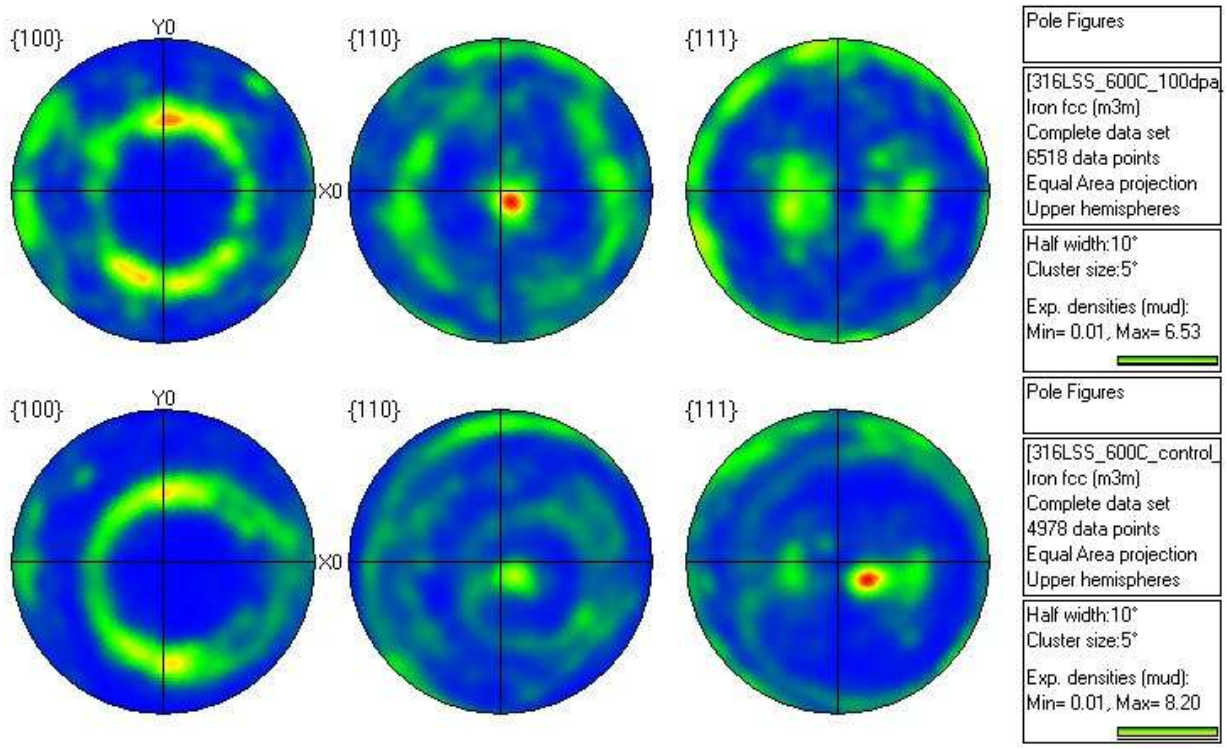

Figure 30. Pole figures of 316L control and 100 dpa irradiated regions.

In order to determine the effects of variation of defect structures as a function depth into the ion irradiation damage, a cross-sectional TEM specimen was quickly prepared by FIB lift-out technique that has become fairly common of a technique. The sample was polished using a low energy cleanup of the film to minimize FIB damage. It was determined looking at Figure 31 and other FIB lift-out samples that the damage produced by the 1 to 2 keV gallium beam produces minimal damage in comparison to the 20 MeV Ni beam. An additional observation for Figure 31 is that microstructural distribution is not uniform and appears to vary, at least in image condition, from one grain to another. The microstructure of ion implantation damaged regions included dislocation tangles, dislocation loops, small voids, and other small defect structures. The density and location of these defects were found to be a function of depth into the sample and ion irradiation conditions.

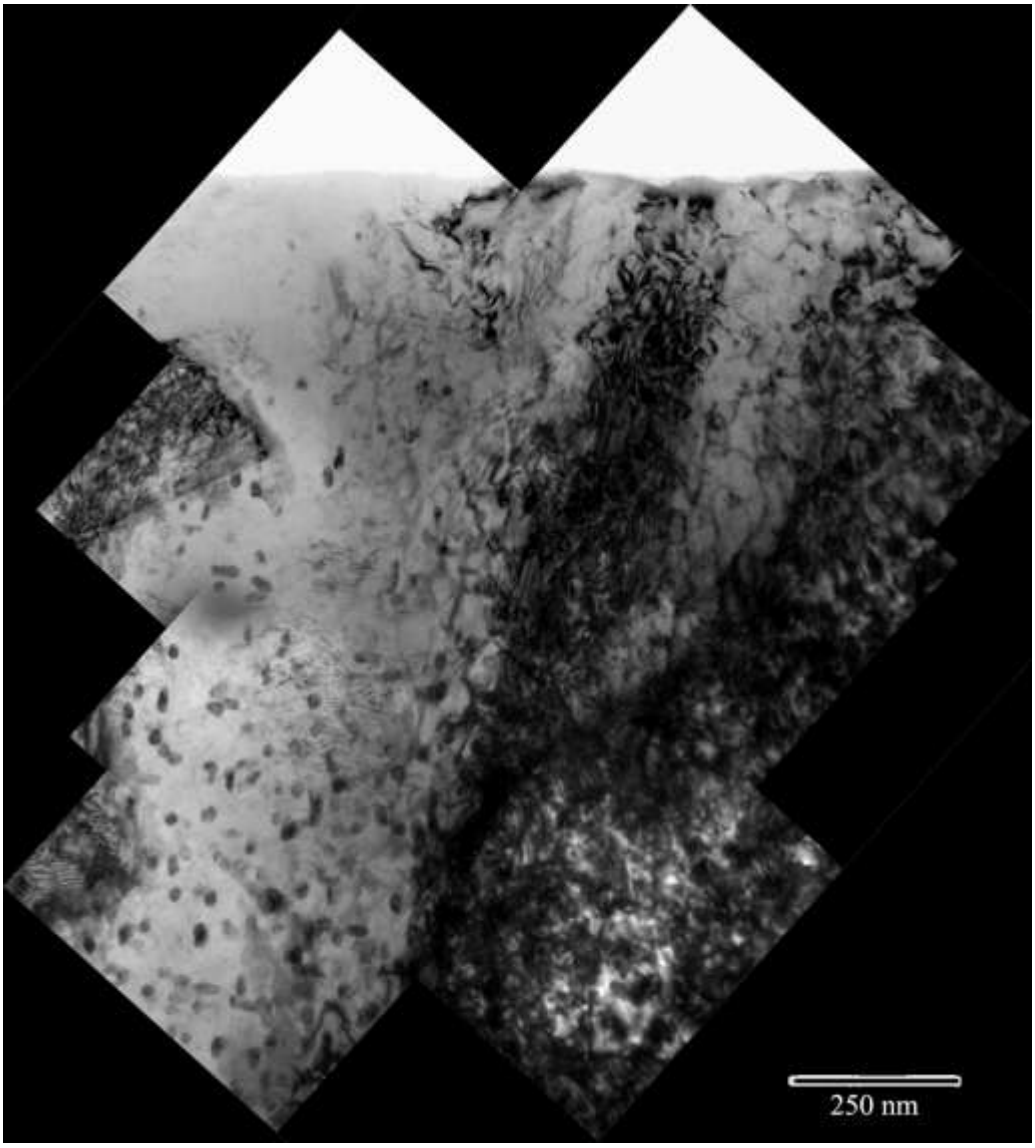

Figure 31. TEM micrograph of the 316L 100 dpa 600 ºC irradiated region as a function of depth.

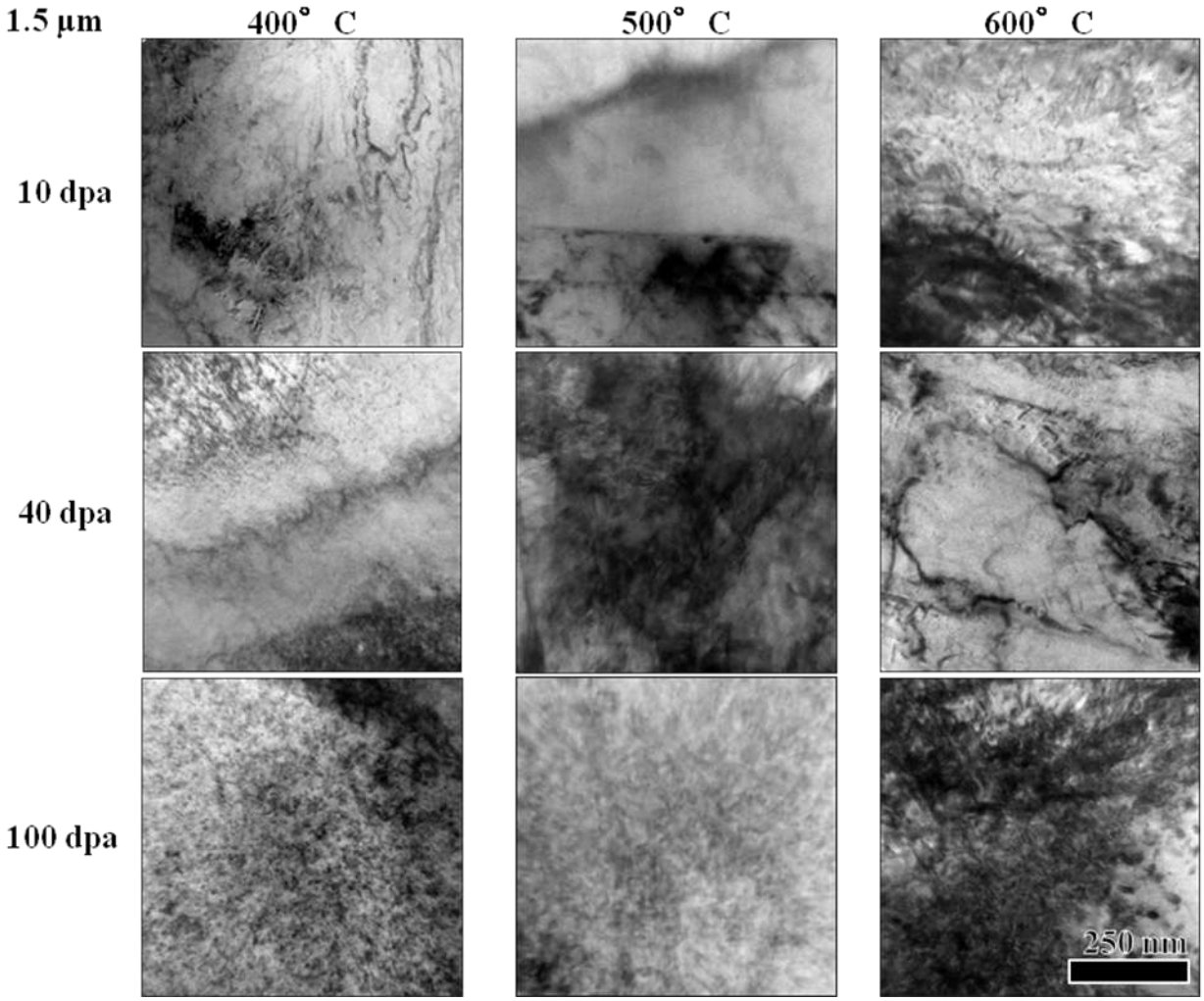

Figure 32. TEM micrographs taken at 1.5 µm into the coupon illustrating the effects of ion irradiation temperature and dose on microstructure.

Beyond a comparison of the defect structure, as a function of depth into the sample a comparison can be made between samples as a function of dose and temperature in the 316L stainless steel. Figure 32 compares all three of the implantation dose and temperatures can be compared. To compare the effects of various implantation dose and temperature, TEM bright-field micrographs were taken at a depth of 1.5 µm below the surface of the original coupon. This region was chosen as the damage profile predicted by SRIM to be relatively flat and it was significantly beyond the denuded region at the surface of the coupon. In comparing the micrographs, the expected trend of increased damage with increasing dose can be seen. The 10 dpa foils show isolated defect clusters that image as black clusters, whereas it is difficult in the 400 ºC 100 dpa image to clearly identify any isolated defect structures. The formation of larger dislocation loops and voids in the high temperature implants provide an explanation for the observed nanoindentation results. It is well known that as the size of the defects increases and the density decreases the force need for a dislocations to pass through the defect field significantly decreases resulting in the decreased hardness between the coupons irradiated at 600 ºC and those at 400 ºC. Despite this effort microstructures are difficult to compare due to the various grain orientations.

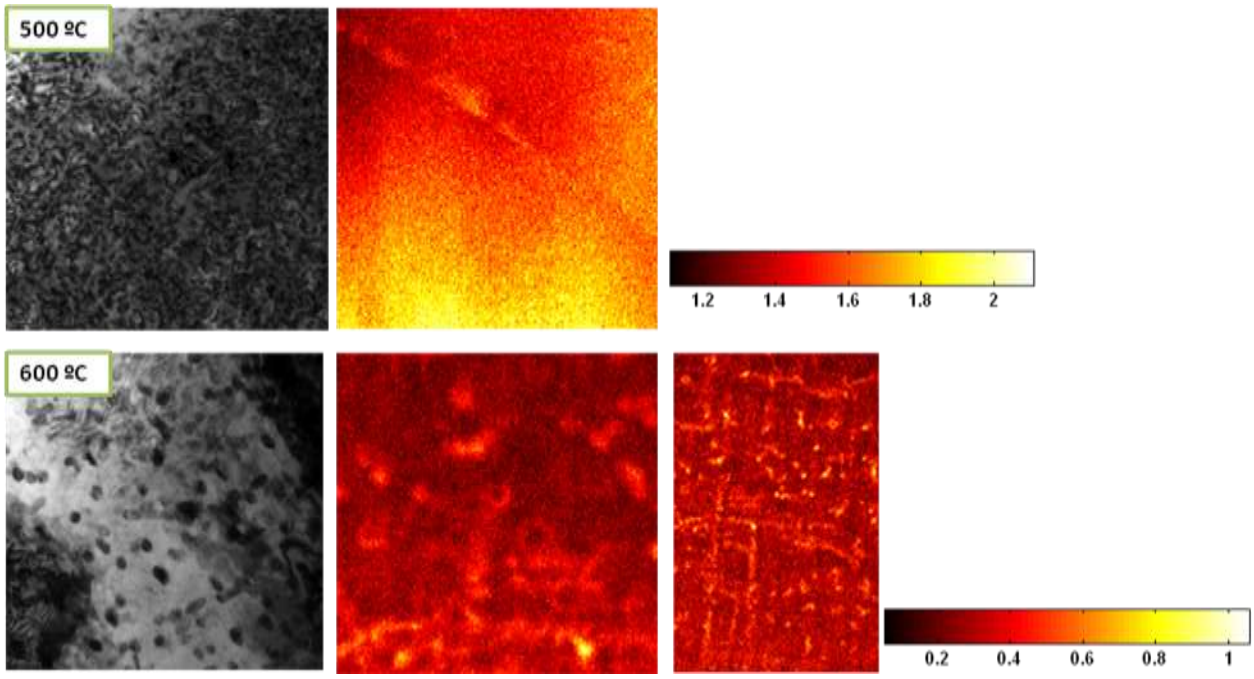

Figure 33. STEM micrograph and EDS maps of the 316L 100 dpa 500 ºC and 600 ºC irradiated region.

To further understand the effects of the ion irradiation on the 316L coupons, energy dispersive X-ray spectroscopy and mapping were performed on the TEM samples. For the majority of the samples, minimal heterogeneity was observed and in those cases was often associated with grain boundaries, as might be expected and can be seen in the example in Figure 33. However in the coupon irradiated to 100 dpa at 600 ºC a significant amount of both Ni and Si solute segregation were observed to occur, as can be seen in Figures 33 and 34.

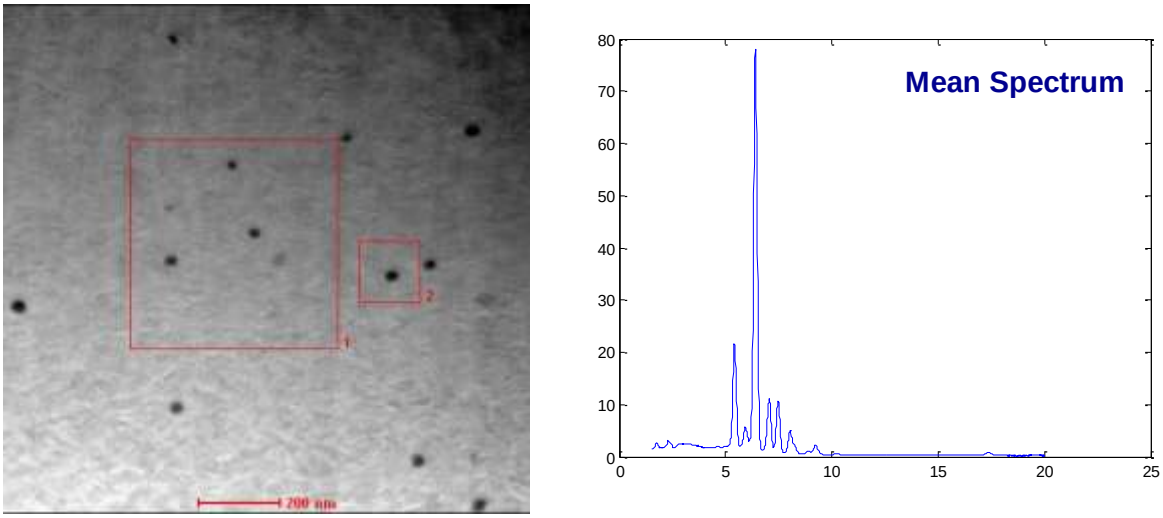

Figure 34. STEM micrograph of the 316L 100 dpa 600 ºC irradiated region and accompaning EDS spectra.

Although the post mortem TEM characterization provides insight into the microstructures that form from radiation damage in these samples, it provides little insight into the mechanisms by which this microstructure evolves under these conditions for such understanding in-situ observation of the microstructure is needed.

5. EXTENSION OF ACELERATED TESTING TO DIFFUSION COUPLES

Diffusion couples provide an excellent tool to investigate in a rapid combinatorial manner the effects of various compositions on the properties of materials. In order for a combinatorial technique based on diffusion couples to be successful, the probe size to investigate the thermal, electrical, or mechanical properties of the material must be smaller to the diffusion range of the material. It was determined based on the length scale limitations already imposed on the rapid characterization technique proposed in this work by the size scale of the ion irradiation that a diffusion couple based production of various alloys would be a feasible way to investigate the effects of various microstructural composition. The limitation of diffusion couples is that it does not consider the microstructure formed by production process, as having a significant effect on the properties and as such results in an uncontrolled key variable in the control of performance of a material properties. [16-19] Despite this limitation, diffusion multiples combined with the proposed characterization technique provides a rapid method to characterize the properties of a large data set of compositions of irradiated materials.

5.1. Production of Diffusion Couples

Diffusion couples for this study were produced by creating a plate of 316L or HT9 with a set of both 6 mm and 18 mm holes produced by end milling the plate. Inserts of refractory metal (tungsten, molybdenum, tantalum, and niobium) plates of 1 mm thickness were placed into the properly labeled slots and covered by 316L plates of 4.5 mm thickness. To induce bonding between the refractory plate and the 316L stainless steel on either side, hot isostatic pressing (HIP) was applied to both the 6 mm and 18 mm structures. The HIP process was followed by a high temperature long duration anneals to induce the diffusion between the refractory metal and the base steel alloy. The resulting 316L plate after HIP and diffusion annealing can be seen in Figure 35 along with a schematic of the sandwich structure created by the HIP procedure. Multiple diffusion couples were then sectioned out of each plate using electrical discharge machining (EDM). The diffusion couple coupons were then mechanical polished down using a final vibratory polish producing a high quality mirror finish.

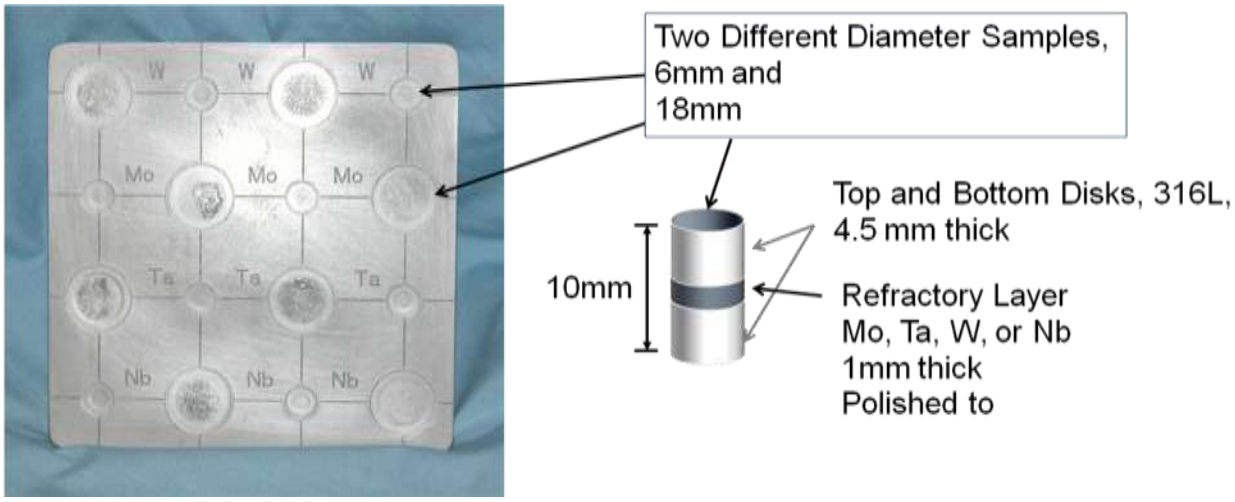

Figure 35. Photograph of the 316L diffusion couple set and a schematic of what the

5.2. Compositional Characterization of Diffusion Couples

Once the 316L diffusion couples for this study were produced by the procedure outlined above, the coupons were analyzed using both SEM and wavelength dispersive x-ray spectroscopy (WDS) techniques. These techniques provided a rapid technique to characterize the interfaces formed from the diffusion couple process. Figure 36 shows an example of the WDS line scan and the SEM image of the tungsten 316L stainless steel couple. A few points to note in the comparison is that the diffusion length scale formed by the coupling is on the order of 10 µm. In both the WDS and SEM images two distinct intermixing regions can be identified by either different slopes in the WDS or different contrast in the SEM image. These are associated with different phases formed. In addition to these regions, a long tail exists in the WDS for the tungsten composition. This portion is the area of greatest practical interest, as it is a stainless steel with varying alloy compositions of tungsten included. Despite this alloy being less than a few percent, it could have an extreme effect on the high temperature and radiation tolerance of the steel.

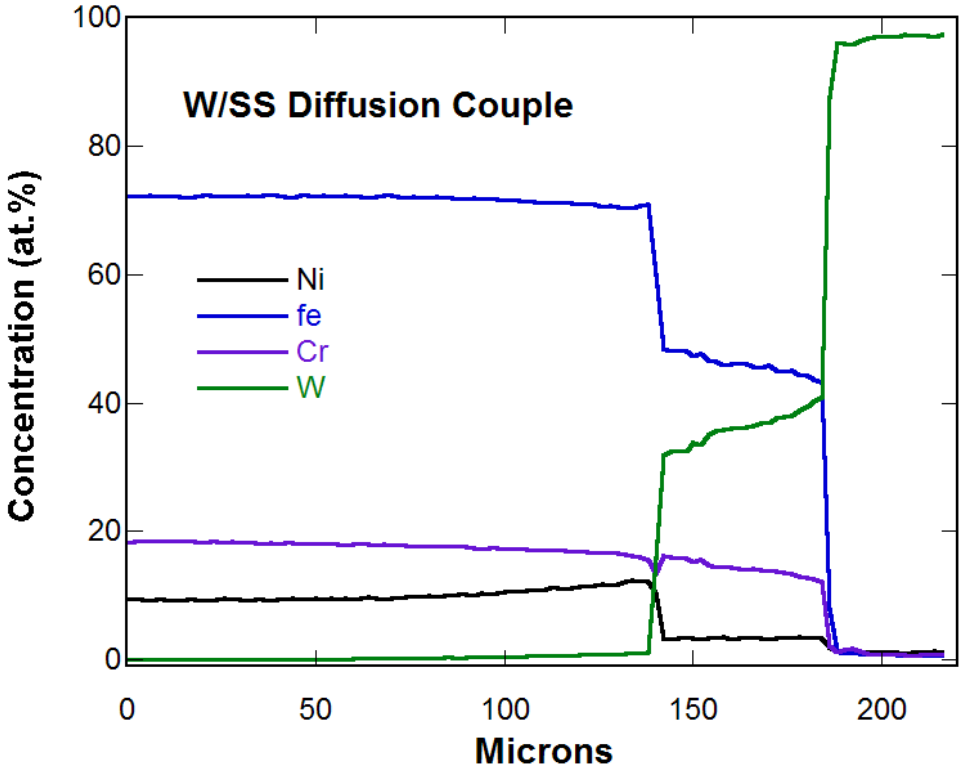

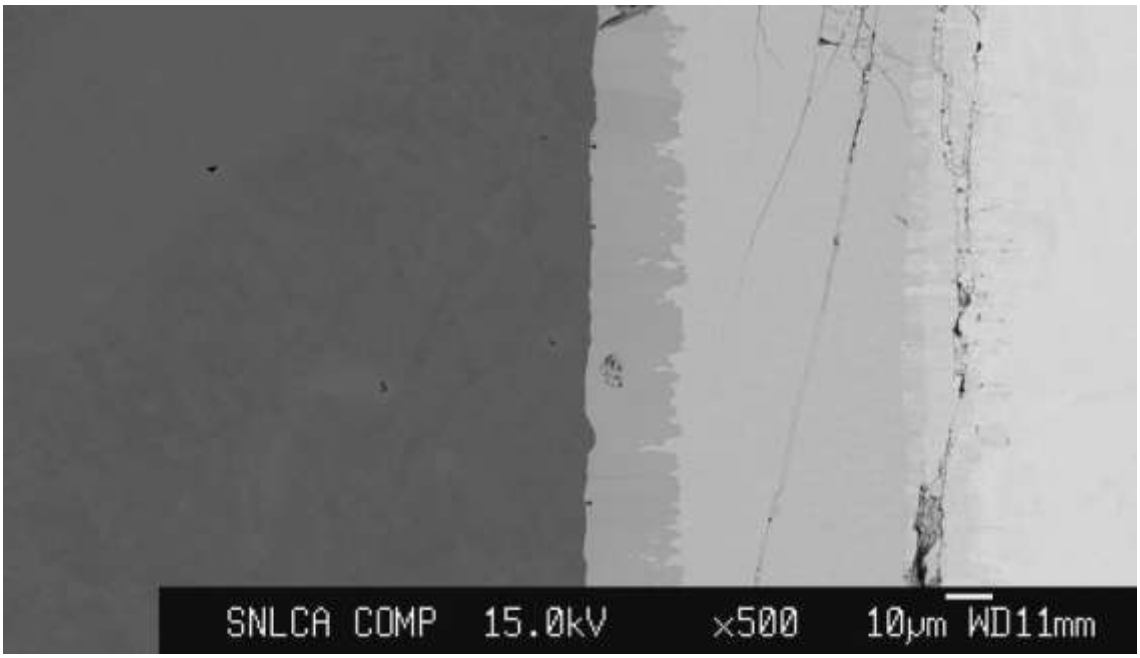

Figure 36. WDS scan and SEM image of the tungsten 316L stainless steel interface

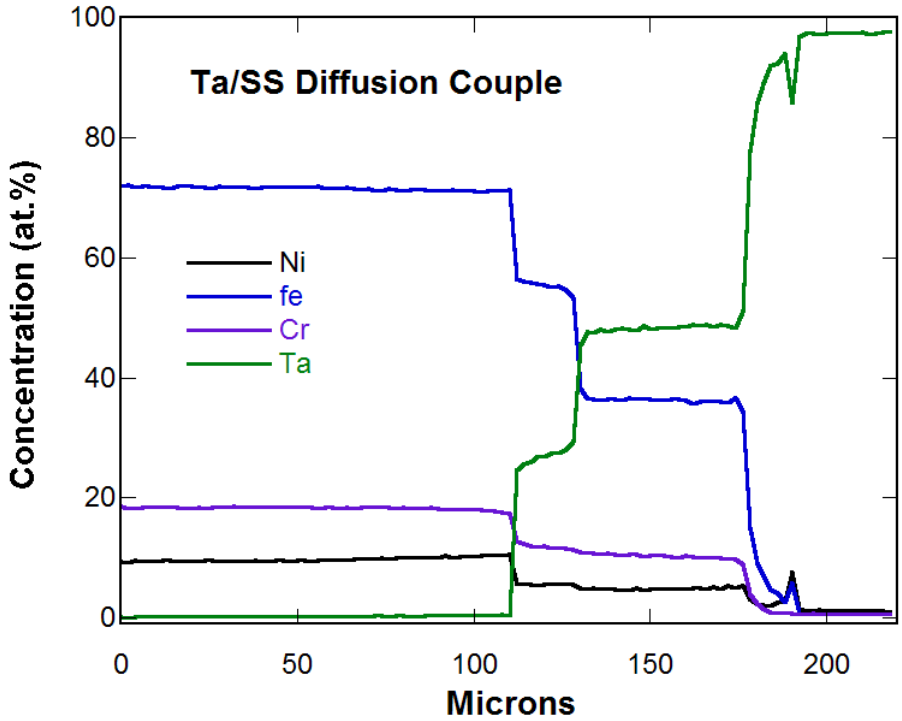

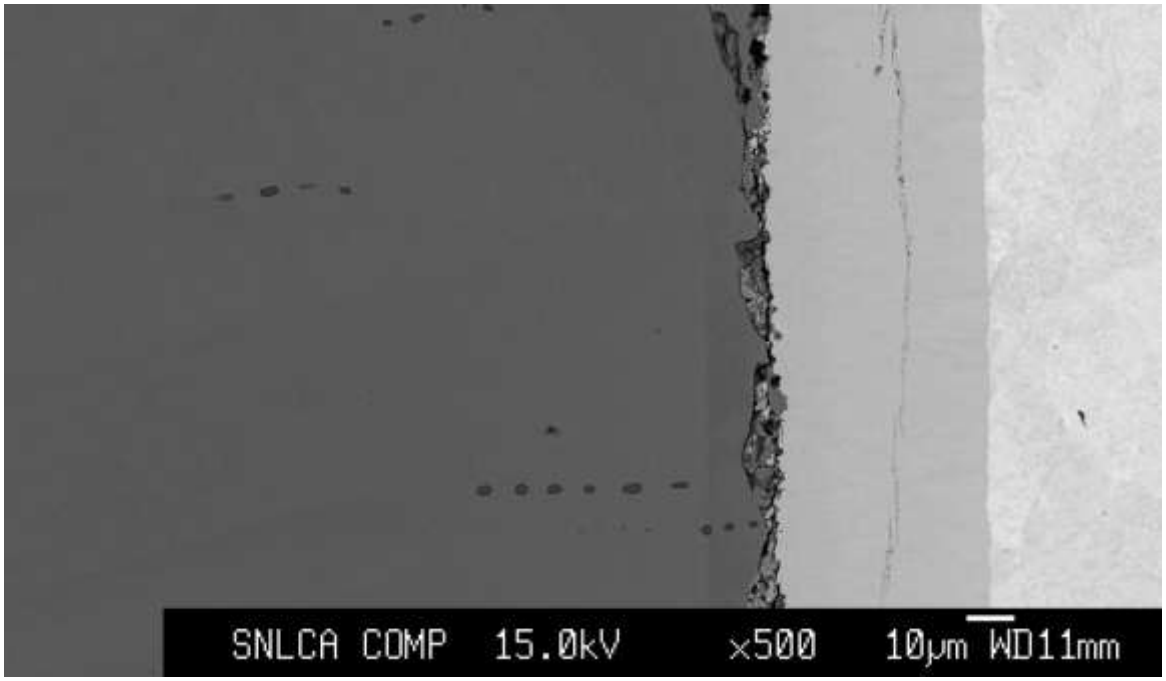

Figure 37. WDS scan and SEM image of the tantalum 316L stainless steel interface

Similar to the tungsten alloy, the tantalum 316L stainless steel demonstrates the formation of distinct phases, in this case three, and a long diffusion tail of tantalum into the steel. In most of these couples cracks can be seen between the various phases. The fact that the tantalum has diffused significantly into the steel suggest that these formed during the long term anneal and not during the HIP process and are thus a result of varying difference in the coefficient of thermal expansion of the various new phases formed.

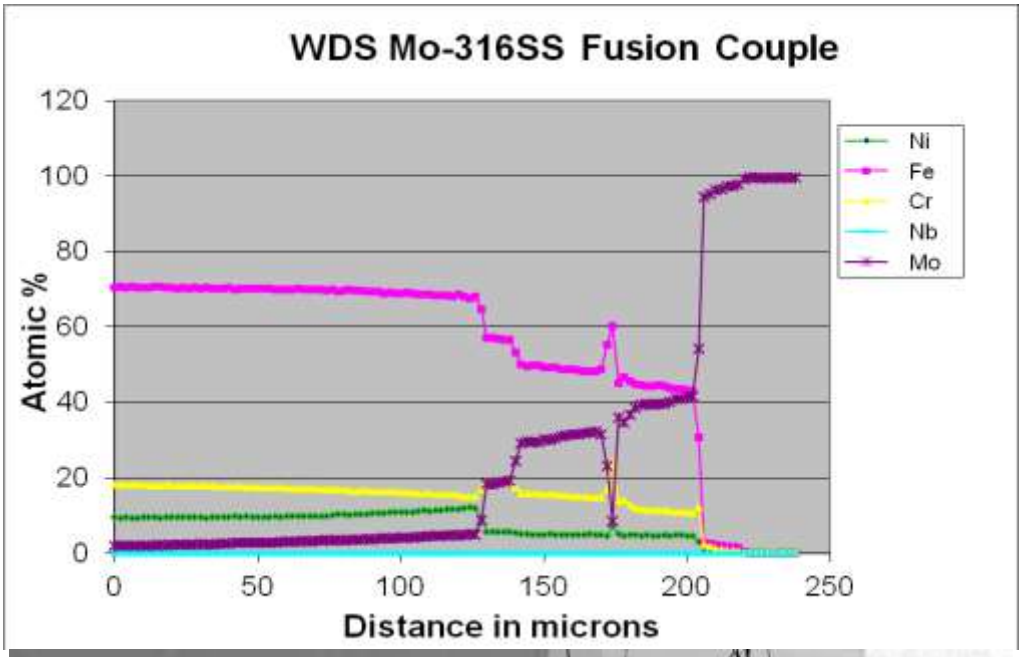

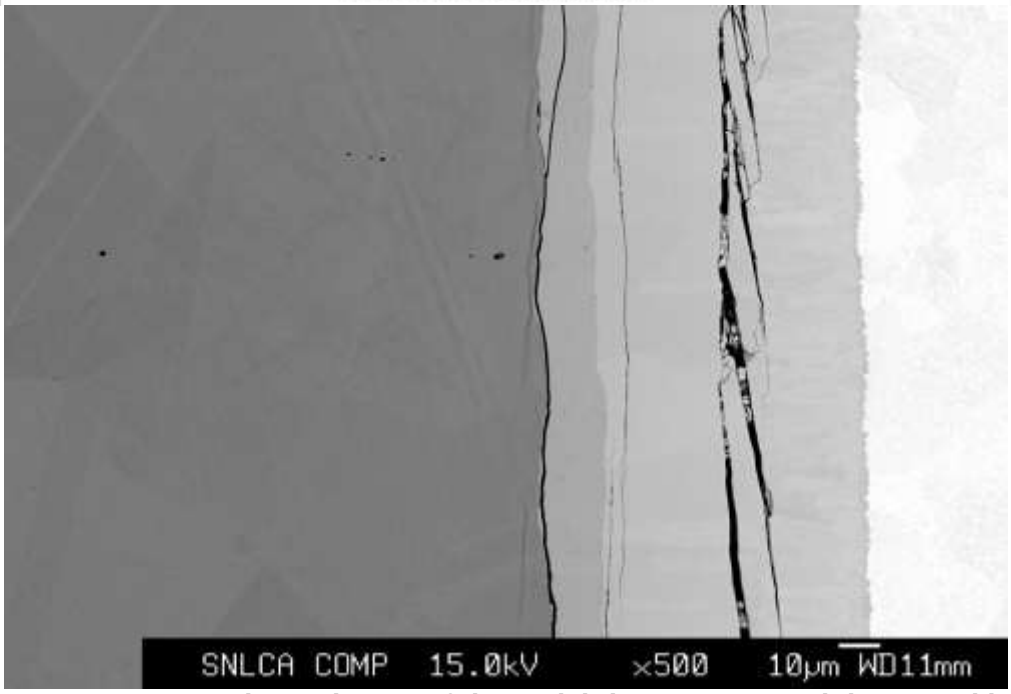

Figure 38. WDS scan and SEM image of the molybdenum 316L stainless steel interface

Figure 38 shows the SEM image and WDS scan for the molybdenum 316L stainless steel couple. It also has a long diffusion tail and the formation of two distinct intermediate phases observed in both the WDS and SEM image. The nature of the cracking in this diffusion couple is such that it results in the blips in the all of the WDS composition profiles. Several of these coupons that were produced required delicate polishing due to the pull out of the region near the crack, the separation failure of the interface, or both.

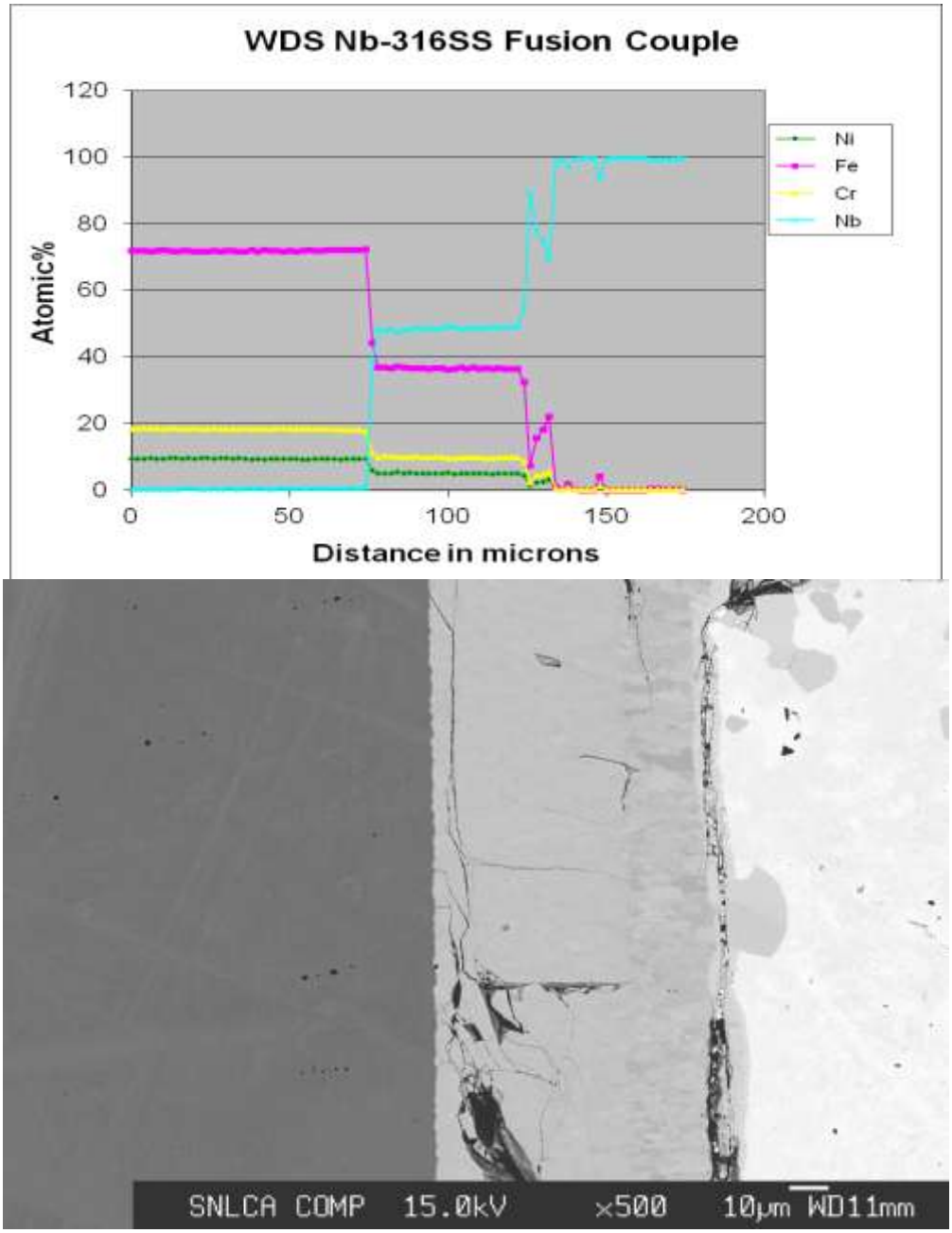

Figure 39. WDS scan and SEM image of the niobium316L stainless steel interface

Finally, Figure 39 demonstrates the WDS and SEM data for the niobium 316L stainless steel diffusion couple interface. It also demonstrated two distinct regions of intermixed region, but had minimal diffusion of the niobium into the stainless steel. Thus suggesting that niobium will not be able to provide much solute capability to the improvement of the properties of the stainless steel. In addition, the cracking in the niobium diffusion couple appeared to be more extensive with cracks propagate not only between phases, but into the intermixing region. The new phases formed also have a much greater difference in niobium concentration resulting in the sharp deference in slope seen in the WDS scan.

5.3. Initial Nanoindentation Testing of Diffusion Couples

The difference in composition that was created by the diffusion couple and characterize in the WDS scans and SEM images in the previous section were then tested using nanoindentation to better understand the resulting change in the mechanical properties of the varying alloy composition.

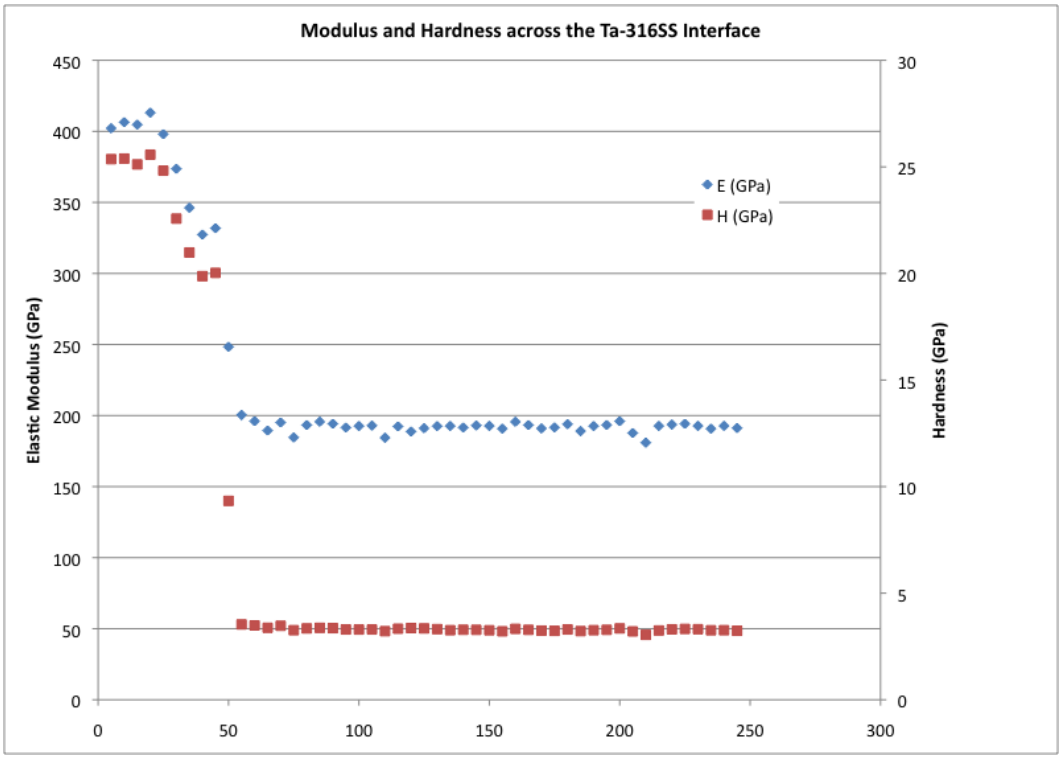

Figure 40. Nanoindentation results across the tantalum 316L stainless steel diffusion couple interface

Figure 40 is a plot of the hardness and elastic moduli from various indentations along the tantalum 316L stainless steel diffusion couple characterized in Figure 37. Both the hardness and elastic moduli show a general linear slop of the property values across the new phases and minimal if any difference in the of properties in the 200 µm area extending into the stainless steel. This suggest despite the diffusion of the tantalum into the stainless steel that can be observed in Figure 37, no observable change can be seen in the mechanical response of the pre-irradiated steel with varying levels of tantalum composition.

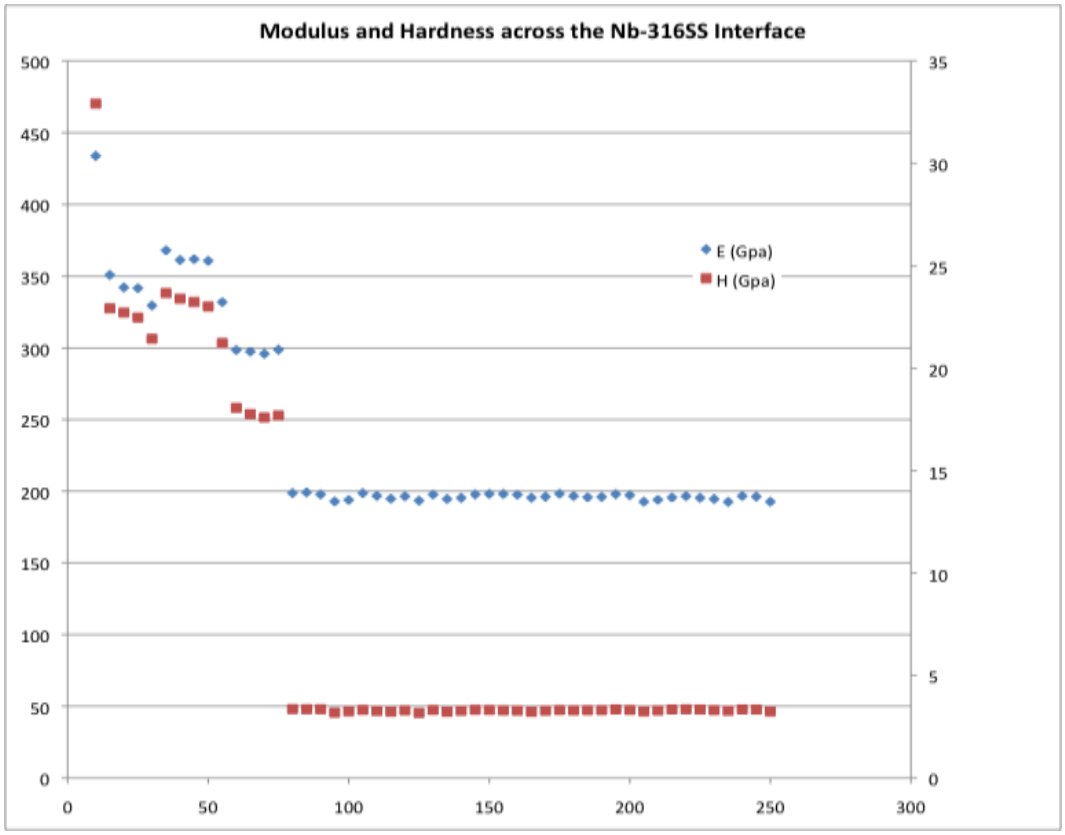

Figure 41. Nanoindentation results across the niobium 316L stainless steel diffusion couple interface

In Figure 41, the nanoindentation results for the niobium 316L diffusion couple vary from that of the tantalum couple in that two distinct hardness plateau can be seen in the new phases that form between the 316L and the niobium. Unfortunately, there does seem to be significant noise in between in the data that might be a result of the cracks that were seen in many of the optical micrographs of the diffusion couples. In addition, there does not appear to be significantly relevant change in the mechanical properties of the region in which the 316L might have absorbed a small amount of the niobium. This suggests that the steel properties were not found to change much even if the niobium was able to diffuse into the steel.

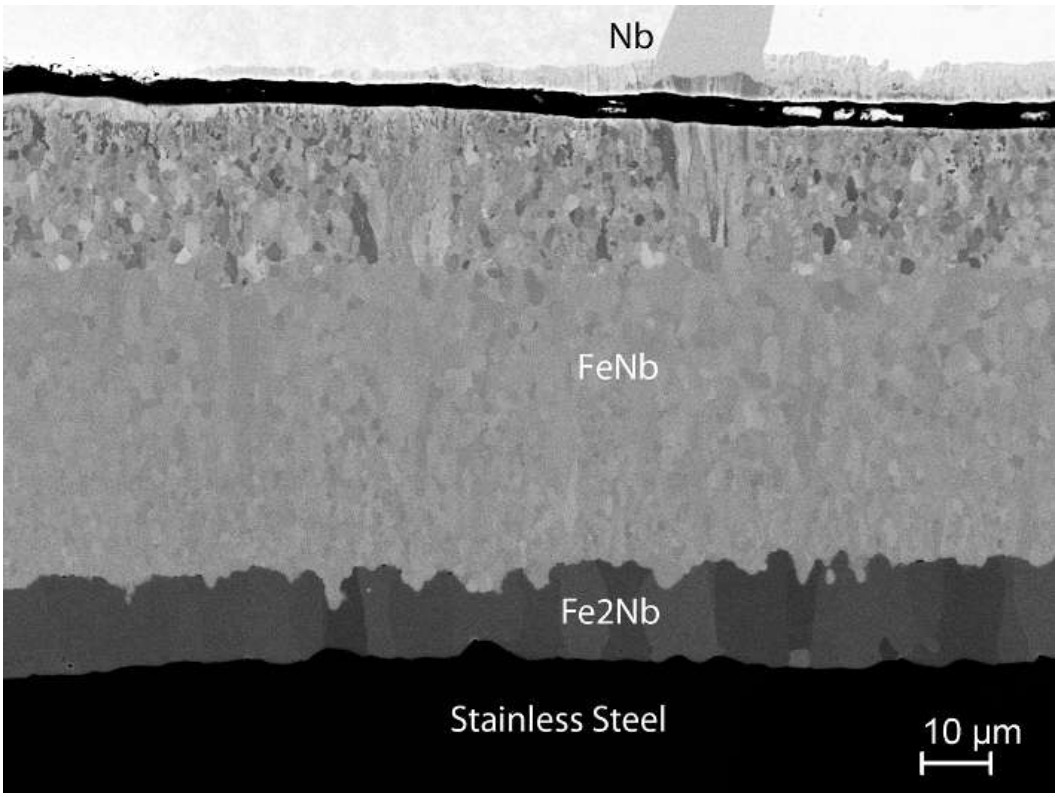

Figure 42 SEM image with the different phases formed in the niobium stainless steel diffusion couple interface

Further characterization of the niobium 316L stainless steel interface was able to identify the region between the niobium and the steel as two distinct phases: FeNb and Fe_2Nb. These two phases were can be clearly identified in the SEM micrograph, seen in Figure 42, with distinct, but not flat interfaces. In addition the grain structure of the different phases can also be observed in the micrograph. The FeNb phase demonstrates a relatively uniform ultra-fine grain size with minimal preference for the diffusion direction. In contrast, the Fe_2Nb phase demonstrates columnar grains running the length of the phase thickness and allying along the diffusion direction. The difference in microstructure between phases and more importantly the changes in microstructure of the stainless steel is an uncontrolled variable in the production of the stainless steel based diffusion couple and something that would have to be studied using conventional samples if a alloy composition of interest was identified.

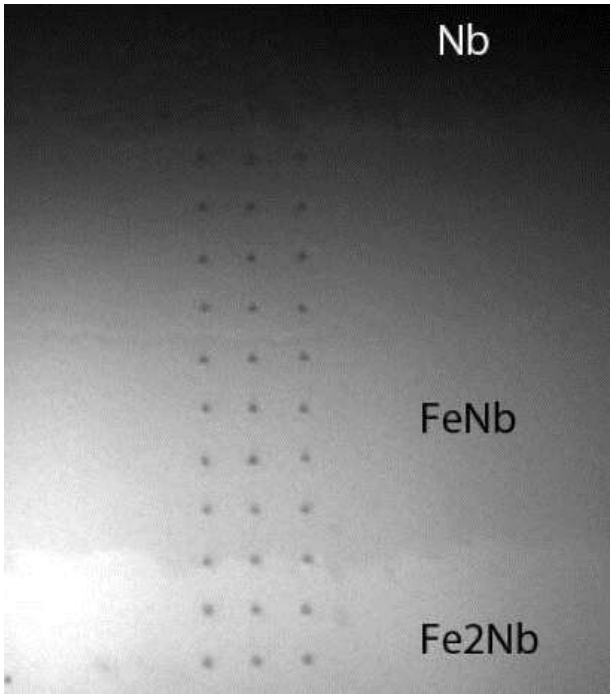

Figure 43. Optical image of the nanoindentation impressions across the niobium 316L stainless steel diffusion multiple interface

The nanoindentation marks remaining after indentation in the niobium stainless steel composition can be seen in Figure 43. Despite the difference in composition and properties of the three phases seen in the optical micrograph there does not appear to be any signs of cracking or varied indentation mark between the Nb, FeNb, and Fe_2Nb phases at the indentation depths tested. This suggests that all of the metal phases had relatively plastic response as expected.

5.4. High-Energy Heavy-Ion Irradiation Conditions

The final stage in the testing of the diffusion couples was the heavy ion irradiation of the diffusion couples using the Tandem accelerator at nominally room temperature to varying dose level. For comparison to previous work, the implantations were done with 20 MeV Ni ions at the maximum achievable dose rate possible by the accelerator on that given day. The spot size was a few millimeters squared. This resulted in a damage rate of approximately 0.003 dpa/s and a end of range of approximately 3.47 µm. In addition, a set of implants were done using a proton beam at 300 keV to t total damage level of 1 dpa and an estimated end of range of 1.32 µm. All of the data presented in Section 5.5 will be on the molybdenum 316L stainless steel diffusion couple for brevity.

5.5. Nanoindentation Testing of Irradiated Diffusion Couples

The results of the nanoindentation results across a diffusion couple that had been proton irradiated was successful completed and can be seen in Figure 44. The hardness values have been separated out based on the depth of the indentation between surface-200 nm, 200-300 nm, 300-400 nm, and 400-500 nm. By doing this, a virtual three dimensional hardness plot is provided. This

was done in an effort to elucidate the effect of end of range on the mechanical property of the film. Although there seems to be a significant amount of scatter in the data, several interesting trends appear to emerge. The first is that the slope in the hardness seen in the non-irradiated coupons as the sample transition between the refractory metal and the steel is maintained and shows no distinct change from that of the pre-irradiated materials. The remainder of the steel with a decreasing molybdenum composition demonstrates a gradual decrease in hardness properties as a function of depth into the diffusion couple with the exception of the data points taken at a depth between 160 and 180 nm into the diffusion couple. This increase in hardness occurs in all of the thickness and in three points suggestive that it is not the result of scatter in the data or faulty result from one indentation. It is possible that this result might be due to local heterogeneity in the region tested and as such further examination is necessary before any conclusive insight can be gained about the increased hardness associated with the composition created 180 nm into the molybdenum 316L stainless steel diffusion couple.

The fact that the hardness is greatest at the top of the 316L sample rather than closer to the end of range suggests that the trend seen with decreased hardness with depth is a result of the work hardening of the relatively soft 316L during the finally stages of vibratory polish used to produce the sample. However, these convoluted effects could not be separated from the difference in the mechanical properties observed between the 316L with molybdenum in it and the new phases formed between the 316L and the molybdenum plate.

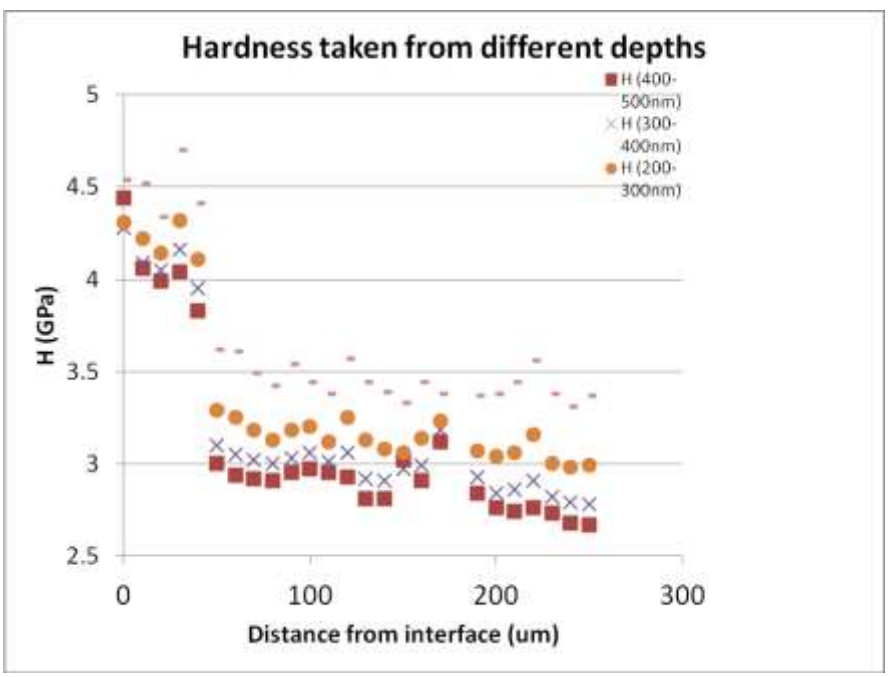

Figure 44. Nanoindentation results across a diffusion couple interface

Figure 45 is the optical image of the nanoindentations into the proton irradiated molybdenum 316L stainless steel diffusion couple. This image shows no significant variation in the indentation size or surrounding region as a function of distance from the molybdenum plate suggesting that all of the material indented to a depth of 500 nm showed similar plastic response and none of the regions appeared to have significant variations in local microstructure that can be observed under the resolving capability of an optical microscope.

Figure 45. Nanoindentation results across a diffusion couple interface

In addition to the proton irradiation, a similar plot showing the three dimensional data can be achieved for the 20 MeV Ni implantations to a damage level of approximately 10 dpa and is plotted in Figure 46. In contrast to the proton irradiation plotted in Figure 44, little distinction in the hardness can be seen between the different phases produced during the manufacturing of the diffusion couple. This further lends weight to the argument that the distinct hardness difference between the 316L and the new phases seen in Figure 44 may be a result of the difference in work hardening response of the new phases and the 316L stainless steel. One of the limited general trends that can be pulled from the scatter of data presented in Figure 46 is that the hardness increases as a function of depth. This suggests that the 20 MeV ion implanted regions shows increased radiation defect structure as a function of increasing depth that provides increased pinning points for the dislocation formed and propagated during indentation. This series of microstructural effects would subsequently result in the increased hardness observed with increasing depth.

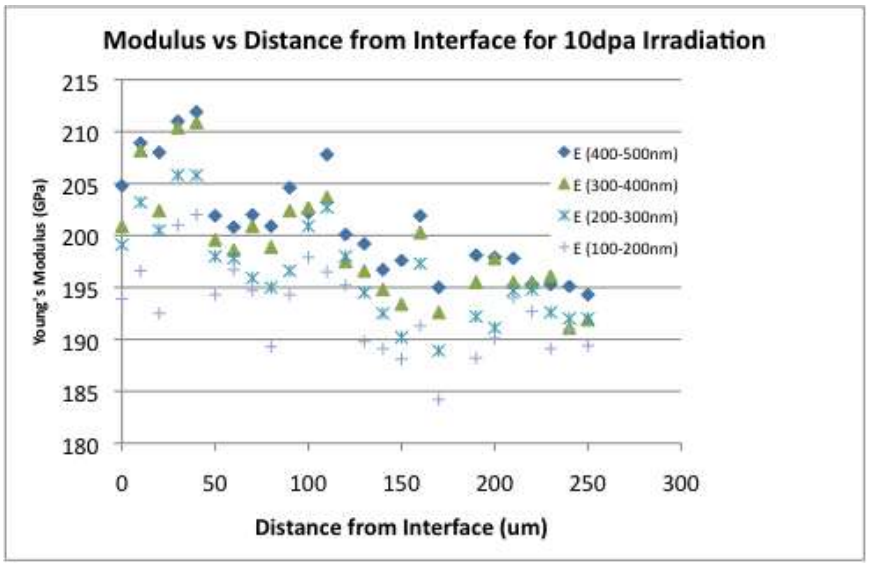

Figure 46. Nanoindentation results across a 10 dpa irradiated diffusion couple interface

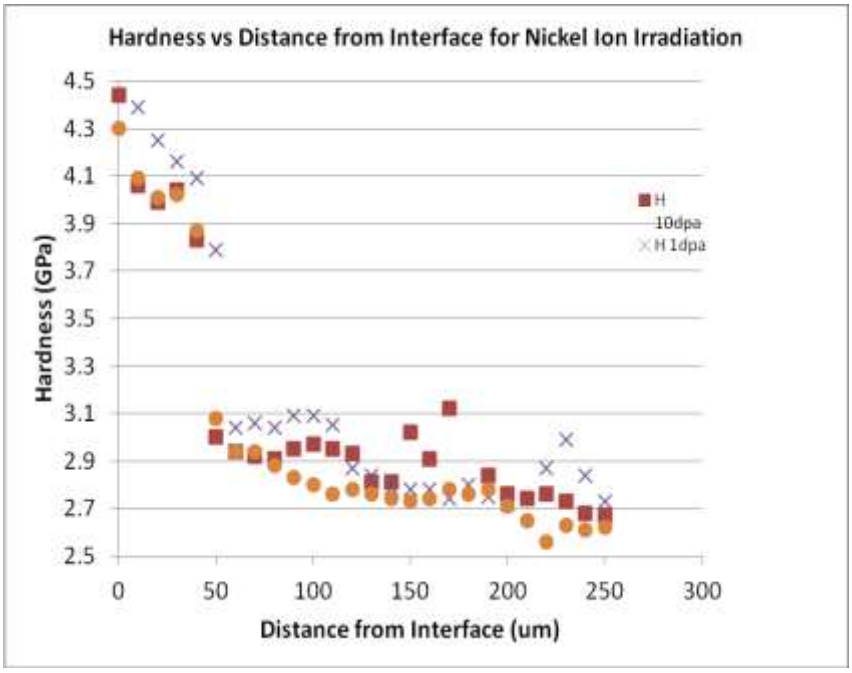

Figure 47. Nanoindentation results across a Ni ion irradiated diffusion couple interface

In addition, to plotting hardness in a three dimensional plot as a function of depth into the irradiated zone and distance from the diffusion couple interface as was done in Figures 44 and 46, a hardness plot can be created comparing the distance from the couple interface and the approximate damage level created in the diffusion couple. This was done in Figure 47 for regions implanted to 1 dpa, 10 dpa, and 100 dpa. When this is done a distinct difference in the hardness of the new phases formed relative to the stainless steel can be observed. In addition, a slight decrease in the hardness of the stainless steel as a function of distance from the diffusion couple interface can be seen in the range between 50 and 250 µm. Although there is significant scatter in the data a region of increase hardness is again observed between 150 and 200 nm from the interface. This region is only present in the regions implanted to approximately 100 dpa, red squares. It is uncertain what factors resulted in this increased hardness in this local region and further studies are planned at naval post graduate school to elucidate this data.

Based on the success of the 316L diffusion couple, diffusion couples of HT9 were produced using similar prepared, characterized, and irradiated using similar techniques. The coupons are currently at the naval post graduate school for nanoindentation and post-irradiation characterization. These findings should provide greater insight into the effects of composition of refractory metals in the mechanical properties and radiation tolerance of metal composition consider for nuclear cladding materials.

6. NEARLY IN-SITU SCANNING ELECTRON MICROSCOPY / ELECTRON BACKSCATTERED DIFFRACTION TECHNIQUE

The extreme environment that is produced in nuclear reactors often results in microstructural evolution of the materials of the reactor, cladding, and associated materials. Understanding how this microstructural evolution occurs is a fundamental aspect of developing superior materials for cladding in future generation of nuclear reactors. A new technique for nearly in situ scanning electron microscopy (SEM) and electron backscattered detectors (EBSD) was developed for a rapid characterization of the microstructural damage that occurs during radiation damage.

6.1. Nearly In-situ SEM/EBSD System Configuration

This project provided the funding for the design and addition of EBSD to the micro-ONE (optical nuclear and electron) beam line on the tandem accelerator. The micro-ONE beam line was designed to have a tungsten tipped filament XL30 SEM aligned parallel to the ion beam line of the tandem accelerator that has the additional optical components to provide a beam spot size ranging from square to micrometer to a few square millimeters. The sample location can be transverse between using a Raith interferometer stage with 10 nm resolution. A schematic of this unique end station can be seen in Figure 48. The green arrows indicate the direction of the electron that are used to create the secondary electron image and the electron backscattered image. The red arrows indicate the path of the ion beam into the chamber and the purple arrow indicates the path of the visible light out of the optical microscope into either a camera or spectrometer. Figure 49 is an image of the micro-ONE beam line with the SEM mounted horizontally on the chamber with the EBSD detector mounted above it. This system provides a unique capability for direct observation of the microstructural evolution that occurs from irradiation damage in a variety of material systems. [20-22]

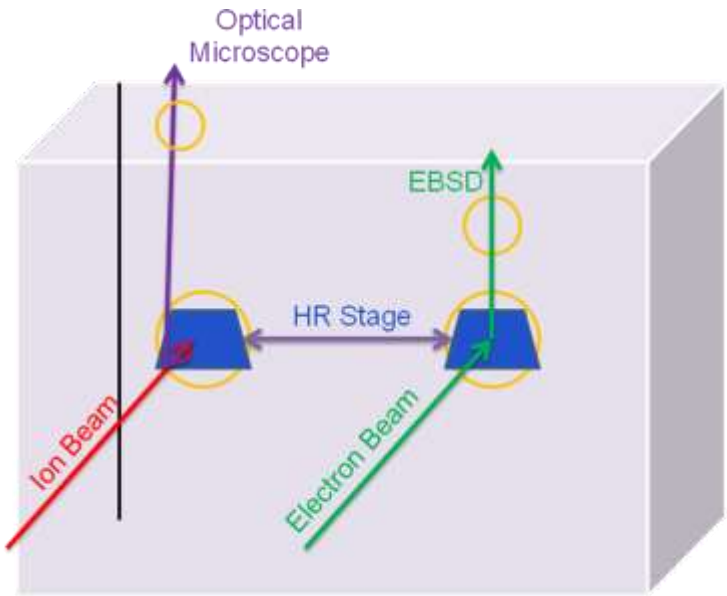

Figure 48. Schematic of the nearly in-situ ion irradiation system on the micro-ONE beam line at the Ion beam Lab

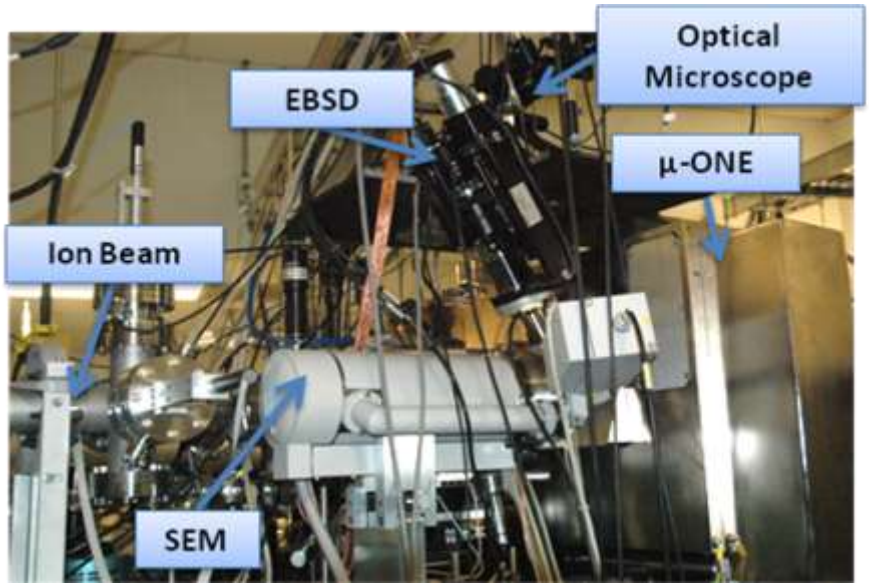

Figure 49. Picture of the micro-ONE beam line with the SEM, optical microscope and ion beam line identified.

6.2. Preliminary Results in an Iconel Alloy

The design required to obtain a proper electron backscattered detector provided a significant challenge that required a coordinated effort between the EBSD producer TSL/EDAX and Sandia National Labs. The instillation of the EBSD into the port of the micro-ONE beam line and the design of an adequate tilting stage were developed, designed, and tested with an Inconel EBSD standard sample. Figure 50 shows a <111> electron backscattered pattern generated from a spot on the sample, as well as an orientation map produced from scanning over multiple grains of the Iconel EBSD standard sample. This result demonstrates the capability to obtain EBSD pattern and map from a horizontally mounted SEM attached to the end station of a tandem accelerator.

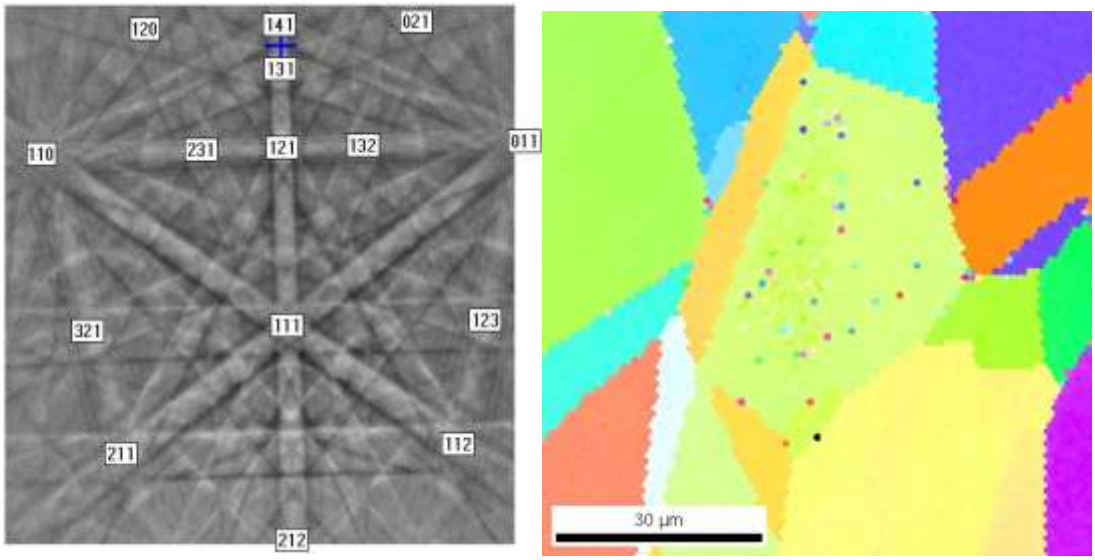

Figure 50. Electron backscattered diffraction pattern and orientation map of a Iconel standard using the EBSD system installed on micro-ONE beam line

7. IN-SITU ION IRRADIATION TRANSMISSION ELECTRON MICROSCOPY TECHNIQUE

In-situ ion irradiation TEM is a technique rich in 50 years of history that has been applied to studying a variety of irradiation conditions. It is a technique that is constantly evolving to incorporate the newest in electron microscopy and ion accelerator capabilities. With the support of this LDRD project, Sandia has joined the short list of elite research institution with the capability to investigate the microstructural evolution that occurs in materials in real time at the nanoscale.

7.1. Need to Understand Structural Evolution at the Nanoscale

Due to the defect size created by radiation damage in most materials, the techniques to characterize the microstructural evolution must also operate at the nanoscale. This requirement leaves a limited number of experimental options to understand the fundamental physics that governs the microstructural evolution of radiation damage in materials from cladding materials in nuclear reactors to single event upsets in microelectronics. The defect clusters formed from radiation damage are also known to evolve as a function of various environmental conditions and material composition and the best way to understand that microstructural evolution is through real time nanoscale observations that is possible through in-situ ion irradiation.

7.2. History of In-situ Ion Irradiation TEM

In situ ion irradiation TEM is a technique that originated 50 year ago in England with the co-emission of electrons and oxygen ions from the tip of a tungsten TEM filament. [23] Since that initial serendipitous observation effort has been made to attach a variety of linear accelerators to a wide variety of TEM. This ranges from focused ion beams attached to intermediate voltage microscopes to tandem accelerators attached to 2 MeV TEMs. These various microscopes-accelerators have been utilized to study the effects of radiation damage in everything from structural metals to microelectronic components. Currently, there exist 11 of these facilities worldwide with the majority being in Japan. In addition to the multiple facilities in Japan, a facility for in-situ ion irradiation TEM are located in China, France, and England each. With the additions of the facility at Sandia partially supported by this project, two facilities now exist in the USA with locations at Argonne National Lab and Sandia National Labs. [24] The locations of the various in-situ ion irradiation TEM facilities can be seen in Figure 51.

Figure 51. A map of the location of in-situ ion irradiation TEM facilities around the world

7.3. In-situ Ion Irradiation TEM System Configuration

The last half of the LDRD project coincided with dedication of the new ion beam laboratory at Sandia and the instillation of the four ion accelerators into the facility. Due to success of the construction team, the building was completed several months ahead of schedule and under budget. $1M of this cost savings was appropriated through a line item change to the purchase and installation of a new ion irradiation TEM. Several microscopes were considered, before a JEOL 2100 TEM was chosen to provide high contrast and tilting capabilities, while being within the budget restraints. The location of the TEM was chosen to be off the 90º left beam line of the Tandem accelerator in the northwest corner of the Tandem target hall. The location is circled in red in Figure 64. It is the only TEM that JEOL USA is aware of that was aligned within a millimeter in five axis. Due to budgetary restraints, a laser curtain was chosen to insulate the TEM from the rest of the Tandem hall. The lighting and HVAC systems were made appropriate for a TEM lab. The room modifications and the stand-alone TEM installation and operation at specifications were completed on January 11, 2011.

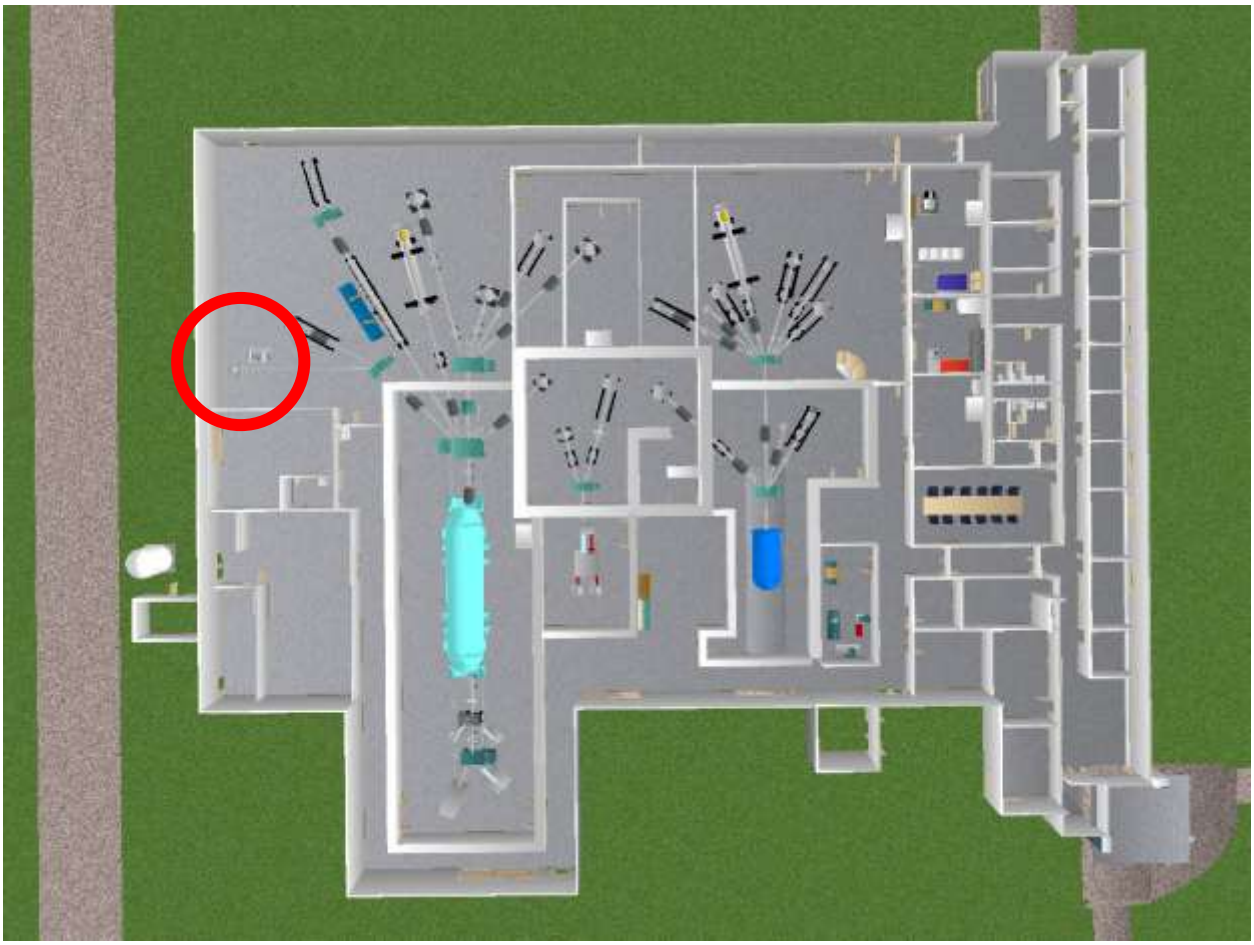

Figure 52. The floor plan for the ion beam lab with the location of the new in-situ ion irradiation TEM indicated.

During the design of the microscope for in-situ ion irradiation studies, the design team considered many specifications, options, and additions to provide the TEM with various sets of capabilities. The final TEM that resulting from the brainstorming sessions would have the following capabilities: 200 kV LaB_6 TEM, ion beams from the tandem accelerator, two Colutron accelerators (one concurrent with the Tandem and the other concurrent with the electron beam), all beams will hit same location, electron tomography, scanning transmission electron microscopy (STEM), nanosecond time resolution (DTEM), procession scanning (EBSD in TEM), *in situ* PL, CL, and IL, *in situ* heating and cooling stage, *in situ* electrical measurement stage, *in situ* straining stage, *in situ* vapor phase stage, and *in situ* liquid mixing stage. By balance budgetary costs associated with each option or addition with the added capability of the system, a plan was develop for a four stage development of the facility as cost permitted. These four stages can be seen in Figure 53. Each generation is associated with the introduction of a new ion beam into the TEM. The instillation of the JEOL 2100 TEM with a maximum voltage of 200 kV LaB_6 filament with the addition of the single electron sensitive camera and active vibration feet was designated as the 0th generation. In this step, the purchase of three stages: *in situ* vapor phase stage, and *in situ* liquid mixing stage, and the tomography stage, were completed. The 1st generation of the in-situ ion irradiation TEM would include the insertion of a collimated ion beam from the 6MV

Tandem accelerator into the TEM through the 0º degree EDX port with all of the required electrical, vibrational, and vacuum requirements required to operate the TEM with acceptable resolution. This was accomplished on April 19th, 2011 with the first beam into the TEM. The 2nd generation of the design will require the insertion of concurrent heavy and light ion beams into the TEM through the 0º degree EDX port that will be produced by the tandem accelerator and a Colutron, respectively. At the time of this report a final design of this system has been determined and construction of the support and vacuum systems has been initiated. During this stage addition dosimetery will be added to provide optical observation of the TEM sample during ion implantation, which may potentially provide the capability for cathodoluminescence and ion beam induced luminescence. The final and fourth proposed generation of the I^3TEM if completed will result in the inclusion of 4 ion beams into the TEM. The fourth addition ion beam will be inserted through a high angle port of the TEM

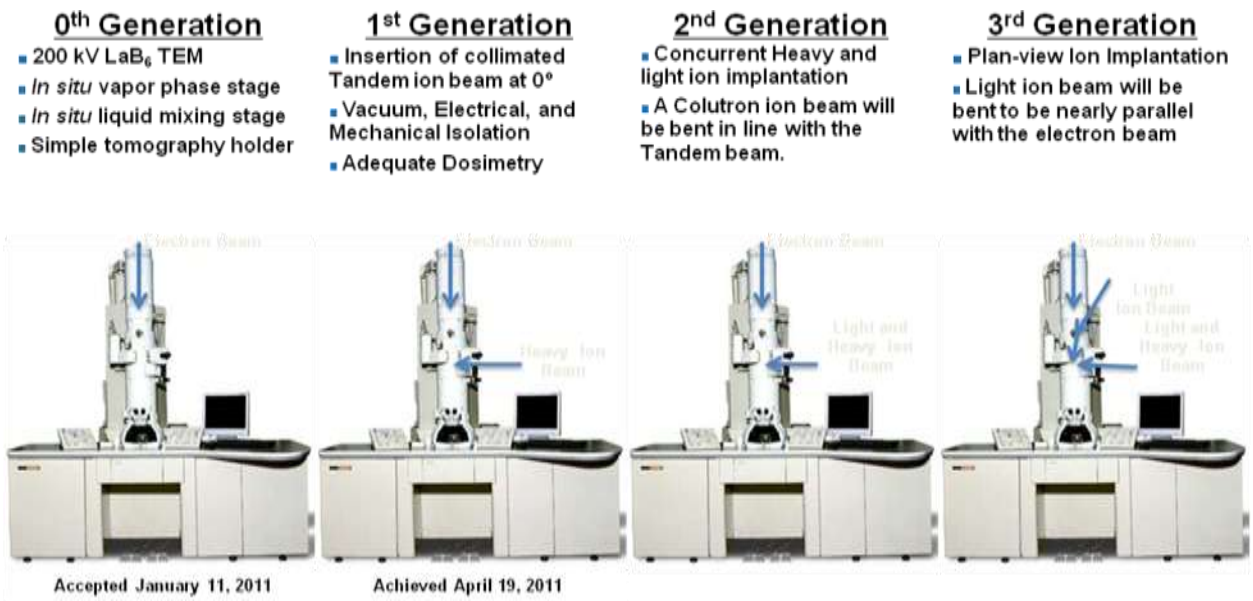

Figure 53. Development plans and current status of the In-situ Ion Irradiation TEM

The first step of the development of an in-situ ion irradiation TEM facility is the installation of a new JEOL 2100 TEM in the ion beam lab. This microscope was selected to have the highest contrast possible through a combination of a wide pole-piece gap and a LaB_6 filament. The TEM instillation was started on October 29th by JEOL technicians assisted by Sandia scientists and Henderson construction crew. According to JEOL USA, this is the first TEM that location was specified to millimeter precision in x, y, and z. Efforts were taken to mitigate local vibration by enhancing the local HVAC system and upgrading the TEM to have both piezoelectric driven stages and active vibration isolation system installed. The TEM was able to meet all of the specification including significantly surpassing the resolution limit by January 11, 2011.

To determine the optimal beam line configuration, Barney Doyle led a simulation effort to identify several proposed beam line configurations. This was done using particle beam optics (PBO) Lab a graphical simulation designed for ion beam line configurations for the particle accelerator community. [25] An ex-

ample of one simulation of the beam line configuration considered in the design of the in-situ ion irradiation TEM beam line can be seen in Figure 54.

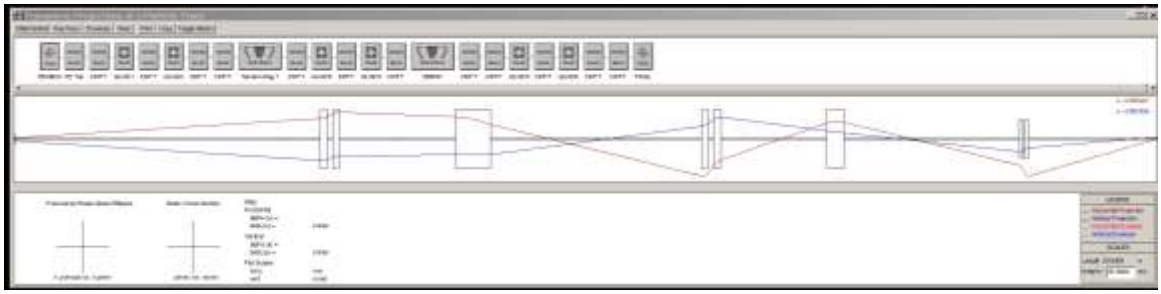

Figure 54. PBO simulation of a beam line configuration considered for the in-situ ion irradiation TEM beam line.

The design developed between to connect the Tandem accelerator to the JEOL 2100 TEM provided several challenges in comparison to most ion beam lines. The location of the TEM in the building required that the port into which the ion beam would enter the TEM be located 90º to the Tandem accelerator requiring two sizable switching magnets. In addition, the desired capability of concurrent heavy and light gas ion irradiation required that consideration be made for later modification to the beam line to accommodate such an upgrade. The greatest challenge in the design of all the in-sit ion irradiation TEMs in the world is providing enough flexibility in the ion steering system to place the ion beam into the 5 mm gap of the objective lens of the TEM with significant dosimetery to know the ion beam location in the TEM.

Based on the PBO simulations, the associated parts were purchased or acquired and the beam line construction was initiated. In addition to the parameters obtained from the PBO lab, the addition of dosimetry and a coupon size chamber were added, as can be seen in the schematic presented in Figure 55.

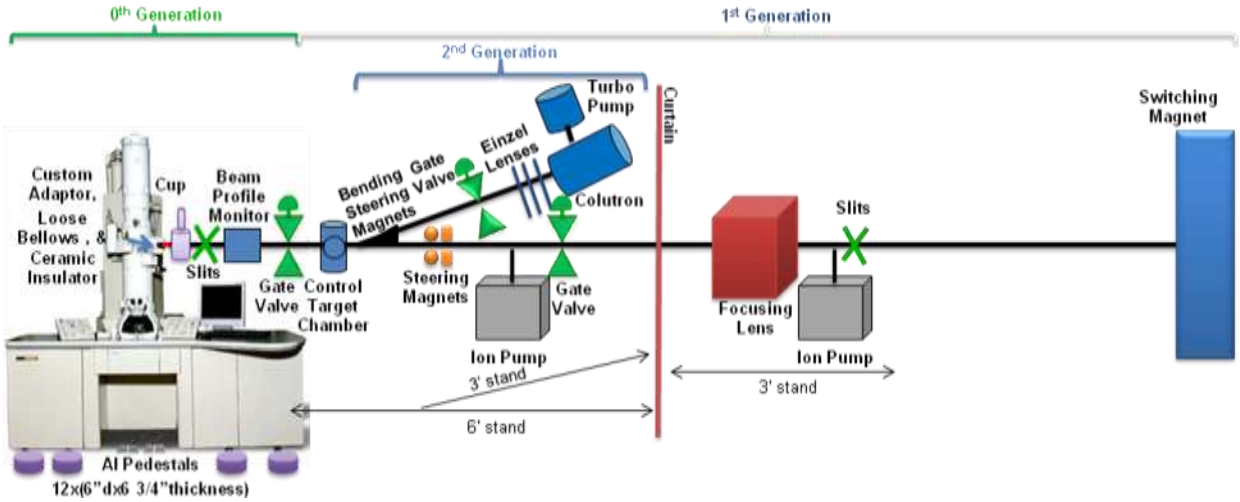

Figure 55. Schematic of the proposed development of the In-situ Ion Irradiation TEM

In additions to the two slits, two switching magnets (only one shown), one steering magnet, and one focusing magnet several other components were designed into the ion beam line to control

vacuum, dosimetery, vibrational stability, and provide added capability. Two ion pumps were included to provide sufficient vacuum capacity for the long beam line and several associated chambers without relying on the TEM vacuum system. For dosimetery, a Faraday cup, and beam profile monitor were included. The Faraday cup was located as close to the TEM as physically possible. In order to minimize the potential vibration along the beam line from the various pumps and mechanical systems associated with the Tandem accelerator and connected beam lines a soft bellow was introduced between the custom TEM-beam line adaptor and the rest of beam line. Once beams can be reliably introduced into the TEM, then initial experiments to provide a proof-of-concept that heavy ion irradiation on the TEM samples produced without cutting, grinding, or polishing could commence.

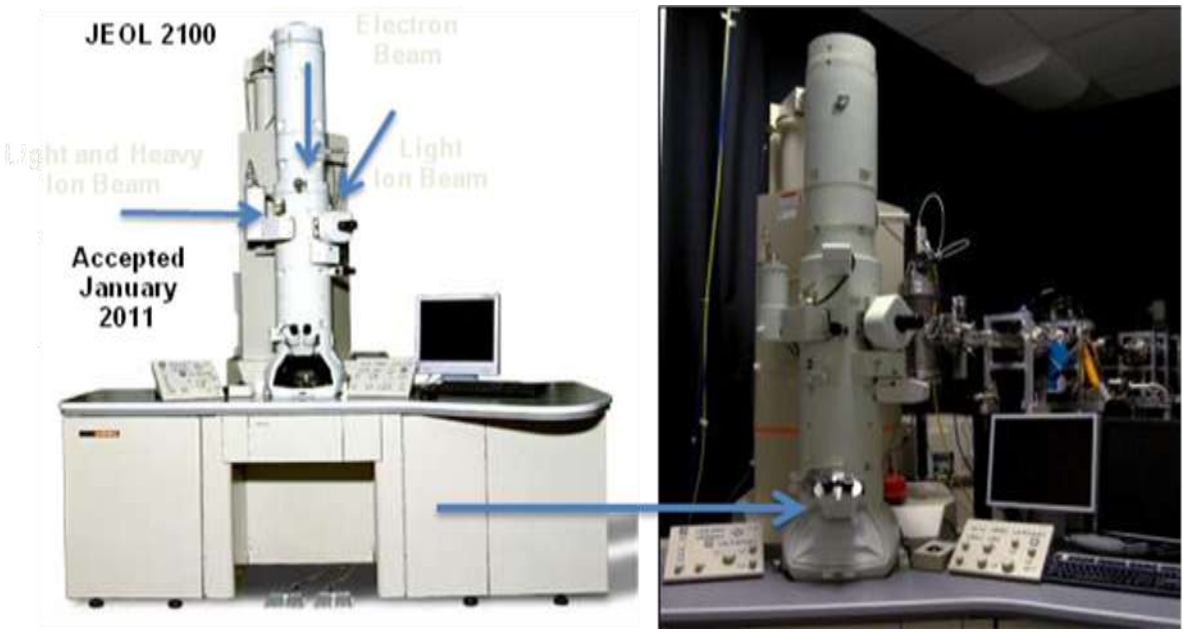

Figure 56. In-situ Ion Irradiation TEM from vision to completed first generation

The in-situ ion irradiation TEM beam line was constructed based on the description in the approach section and the schematic in Figures 54 and 55. The vacuum system was found to be better than anticipated resulting in a significant improvement when the gate valve separating the TEM and the beam line was open. With this beam line configuration, beam current was recorded on a TEM Faraday stage on April 19, 2011. Despite this initial success the beam current was found to be inadequate for the planned experiments.

As a result, several subsequent iterations were undertaken to optimize the beam line design. To improve the vacuum system, two additional gate valves were added and an access port for leak checking the system. One of the gate valves was directly vicinal to the last switching magnet to protect the other beam lines and Tandem during maintenance of the beam line. The other was placed between the Faraday cup and the bellow to minimize the volume the TEM pumps would have to handle during non-irradiation experiments. The dosimetry was also found to be inadequate resulting in a requirement of up to eight hours for ion beam alignment. This is currently being rectified by several measures. A beam profile monitor was added upstream of the first set

of slits permitting characterization of the beam after the 90º bend provided by two switching magnets. The unsuppressed Faraday cup was replaced with a suppressed Faraday cup and a Quartz and phosphor viewing screen. The suppressed Faraday cup permits accurate current measurements prior to the insertion of the ion beam into the TEM. The addition of the viewing screen with both quartz and phosphor slides permit direct observation of both high and low current beam locations and sizes prior to the ion beam insertion into the TEM.

A Faraday TEM stage was initial used for the final dosimetery in the TEM, but was found to be inadequate. The stage designed for measuring the current from an electron beam did not have adequate suppression to align the ion beam. As a temporary alternative, paper and tape burns were used to identify the location of the ion beam on the tilted TEM stage prior to experimentation on the sample. The introduction of soot into the TEM resulted in significant degradation of the TEM vacuum system requiring regular bake outs that subsequently degraded the TEM alignments. A variety of long term solutions were considered including the insertion of a quartz and CCD directly across from the ion beam through a redesigned Faraday TEM stage. It was determined that the best option was to create a line of sight path to directly observe the TEM stage optically during ion irradiation. A company, Integrated Dynamics Electron Solutions, willing to provide this significant modification to the TEM under conditions that meet both Sandia radiation safety standards and JEOL TEM specification was identified. An order was placed and the modifications are currently in process. Once complete the dosimetery for the in-situ ion irradiation TEM beam line should be adequate for both the 1st and 2nd generation of the proposed beam line.

During the optimization of the beam line, several ion beams were introduced into the TEM including 1.7 MeV Au3+, 2.5 MeV H+, MeV He+, 3 MeV Si3+, 3 MeV Cu3+, 3 MeV Au 3+, and 14 MeV Si+. The maximum possible beam current increased with both experience with each irradiation condition and beam line modification increasing from approximately 10 pA to 200 nA. The current configuration of the in-situ ion irradiation TEM can be seen in Figure 56.

7.4. Preliminary Results

To prove the feasibility of applying in-situ ion irradiation technique to the study the microstructural evolution of advanced cladding materials using the facility that was in development at Sandia, Dr. Marcus Kirk at Argonne National Lab was gracious enough to permit the in-situ ion irradiation of a steel sample at their facility. [26-29] This permitted both discussions on the best design of the facility and the optimal experimental conditions for a variety of conditions, as well as a preliminary study of 1 MeV krypton ions using the intermediate voltage TEM facility for in-situ ion irradiation facility at Argonne. The initial results from these experiments can be seen in Figure 57. The effects of ion irradiation can be observed to alter the dislocation pile-up structure seen in the steel as dislocation loops produced from the irradiation damage interact with the preexisting dislocation structure. These results show that microstructural evolution of possible cladding materials can be investigated using the facility that is being developed at Sandia.

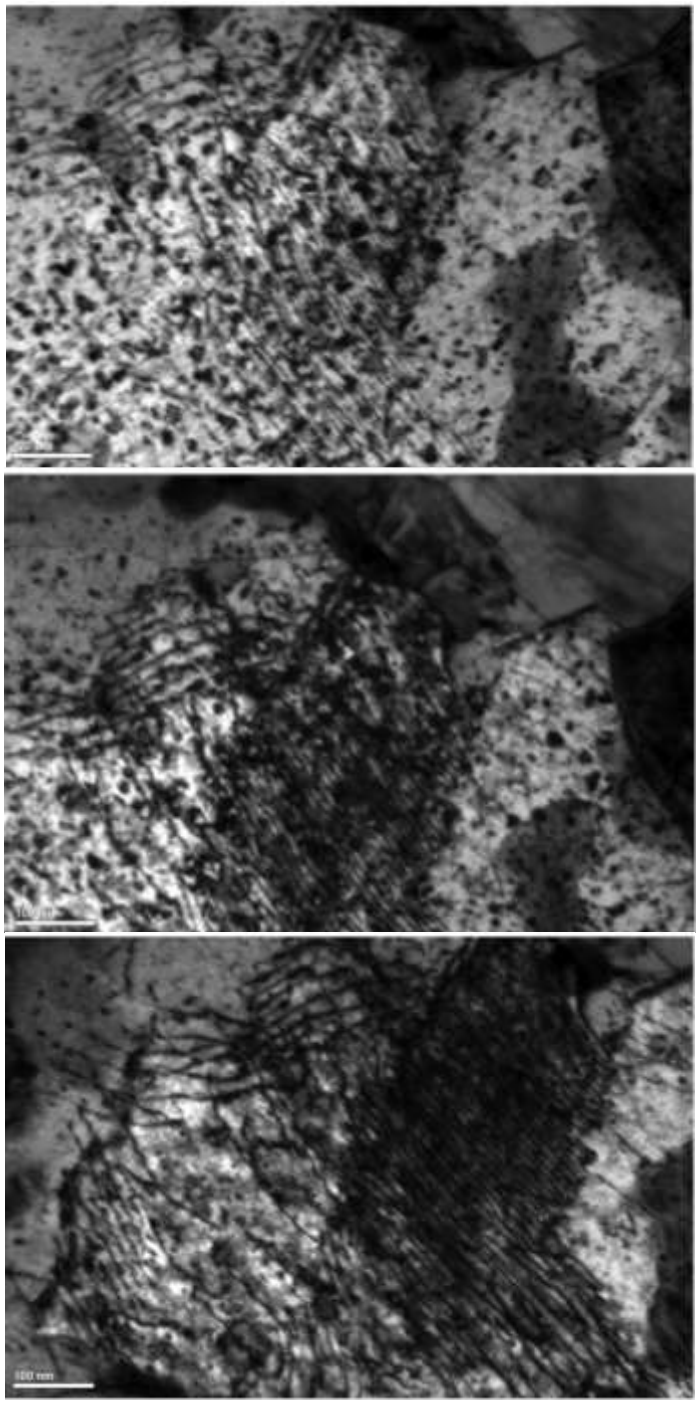

Figure 57. Images of defect structure evolution in ion irradiated steels performed at IV-TEM and Argonne National Laboratory

7.5. Future Direction and Planned Collaborations

Although this technique shows promise as a very rapid technique to screen for materials that are resilient to extensive radiation damage, it raises many concerns that needed to be addressed if it

is ever applied to advanced materials. The first concern is the volume of the small scale testing technique chosen. It must be significantly smaller than the irradiation volume, but significantly large enough to average over the heterogeneous microstructures of the sample. Nanoindentaion was found to provide this capability in a rapid fashion and as such was chosen over other techniques like micropillar compression. The selection of the ion species and energy is important to provide heavy displacement damage, minimal compositional variation, and a deep flat damage profile. Although the choose of Ni did provide extensive displacement damage and minimal alteration in composition of the 316L steel, it did not provide an extremely deep and flat distribution of defects making too difficult associate the recorded hardness with an observed microstructural region. In addition, Ni ion beam has been indicated by others to have additional adverse effects when implanted into steels and thus provides a poor chose. Finally, the use of heavy ion irradiation alone does not provide any insight into the bubble formation, swelling, blistering, and hydrogen embrittlement that are observed in neutron exposure. A significant representation of any of these effects alone can result in the exclusion of a material system from consideration.

Current work is underway to better understand the microstructural evolution and the resulting effect on mechanical properties to further refine the proposed method to rapidly characterize to a first-order the viability of new structural metals for extreme radiation environments. Work is also underway to capitalize on the small scale nature of the irradiation and testing by reproducing this works on various 316L and HT9 based diffusion multiples. Finally, work to incorporate a distribution of hardness either from the distribution of various defect structures provided by TEM or through SRIM calculations into the FEM has been initiated.

The success of this project has resulted in many scientists both internal and external to Sandia being interested in continuing the research and utilizing the new capabilities developed by this LDRD project. The capability to produce micropillars at Sandia that was initiated by this project has already been utilized by Corbett Battalie, Brad Boyce, and others to investigate strength in metal tribofilms and various other materials. [30] The nearly in-situ SEM/EBSD ion irradiation capability is of interest to Prof. Mitra Taheri's group at Drexel University, as they investigate texture evolution in grain boundary engineered alloys for future cladding materials. In addition, multiple groups from both other national laboratories and various universities have initiated discussion and in some cases research utilizing the in-situ ion irradiation TEM. For example, Amit Misra at Los Alamos National Lab has initiated research into the radiation tolerance of the copper-niobium interface using the I^3TEM. Similarly, Prof. Julia Greer at Cal Tech's group are in the process of ex-situ TEM characterization of ion irradiated nanoscale tensile bars and are planning on following up to determine the active mechanisms using the I^3TEM. Prof. Emmanuelle Marquis' group from University of Michigan has also initiated a collaboration to investigate the effects ion irradiation on the segregation of tungsten-ruthenium alloys using atom probe tomography and the I^3TEM.

Effort to solicit follow on research has resulted in the successful development of a nano-to-micro LDRD proposal on the degradation of nuclear waste fuels and cladding stored in dry storage. Additional efforts have also resulted in meetings with both the DOE-BES and DOE-NE to support the development of the interesting and high potential collaborations, but with no addition funding provided to date. Because of the large interest, efforts will continue to further develop these capabilities and collaborations, as well as the proper funding to support them.

8. CONCLUSIONS

The conclusion of this LDRD project is that heavy-ion irradiation combined with small scale mechanical testing and TEM characterization can be used to provide a rapid characterization of the microstructure and mechanical properties of various metal compositions being considered for extending the life-time of current reactors and those proposed for the next generation of reactors. In order to successfully provide this first screening experimental technique, the effects of length scale, ion irradiation rate, sample preparation, and microstructural heterogeneity must be taken into consideration. To provide rapid subsurface microstructural characterization FIB-based TEM lift-out was shown to elucidate radiation damage from the 20 MeV ion beams that is distinguishable from the few keV Ga beam used in the sample preparation. Despite these concerns, sample preparation, irradiation, microstructural analysis, and mechanical property characterization can currently be done in about a week time period.

In addition to proving the feasibility of this technique, this LDRD has left Sandia with three new capabilities that can benefit a variety of projects. These include micropillar compression, nearly in-situ ion irradiation SEM/EBSD, and in-situ ion irradiation TEM. These micropillar compression technique combined with nanoindentation provide a method for characterization of a variety of microstructures within the limitation of the ion irradiated region. The nearly in-situ ion irradiation SEM/EBSD provides information on the surface texture as a function of implantation dose, which can be of great use in samples that exhibit grain boundary motion or large scale segregation as a result of the radiation damage. Finally, the in-situ ion irradiation TEM is a very unique instrument that provides real time nanoscale observation of defect mobility during ion irradiation. As a result of its capabilities, it has generated subsequent interest both internal and external to Sandia. The addition of these three new techniques and the promising screening methods for potential new materials for nuclear reactor claddings has made this LDRD a success.

9. REFERENCES

1. Jiao, Z., J.T. Busby, and G.S. Was, *Deformation microstructure of proton-irradiated stainless steels.* Journal of Nuclear Materials, 2007. **361**(2-3): p. 218-227.
2. Zu, X.T., et al., *Effect of proton and Ne irradiation on the microstructure of Zircaloy 4.* Philosophical Magazine, 2005. **85**(4-7): p. 649-659.
3. Kai, J.J. and G.L. Kulcinski, *14 MeV nickel-ion irradiated HT-9 ferritic steel with and without helium pre-implantation.* Journal of Nuclear Materials, 1990. **175**(3): p. 227-236.
4. Plumton, D.L., G.L. Kulcinski, and R.A. Dodd, *Phase transformations in ion irradiated Ti-6242s alloys.* Journal of Nuclear Materials, 1987. **144**(3): p. 252-263.
5. Zee, R.H. and G.L. Kulcinski, *Disordering of CuPd by 14 MeV copper ions.* Journal of Nuclear Materials, 1986. **141-143**: p. 878-882.
6. Zinkle, S.J., R.A. Dodd, and G.L. Kulcinski, *Ion irradiation of high strength, high conductivity copper alloys at fusion-relevant temperatures.* Journal of Nuclear Materials, 1985. **133-134**: p. 680-684.
7. Ohta, J., et al., *Hardness of 12Cr-8Mo ferritic steels irradiated by Ni ions.* Journal of Nuclear Materials, 1995. **225**: p. 187-191.
8. Sindelar, R.L., G.L. Kulcinski, and R.A. Dodd, *Depth dependent microstructure in ion-irradiated 316 type steels.* Journal of Nuclear Materials, 1984. **122**(1-3): p. 246-251.
9. Sindelar, R.L., G.L. Kulcinski, and R.A. Dodd, *Heterogeneous void formation in 14 MeV nickel-ion irradiated 316 SS.* Journal of Nuclear Materials, 1985. **133-134**: p. 544-548.
10. Maass, R., et al., *A strong micropillar containing a low angle grain boundary.* Applied Physics Letters, 2007. **91**(13).
11. Uchic, M.D., P.A. Shade, and D.M. Dimiduk, *Micro-compression testing of fcc metals: A selected overview of experiments and simulations.* JOM, 2009. **61**(3): p. 36-41.
12. Fischei-Cripps, A.C., *The sharpness of a Berkovich indenter.* Journal of Materials Research, 2010. **25**(5): p. 927-934.
13. Fischer-Cripps, A.C., *Review of analysis and interpretation of nanoindentation test data.* Surface & Coatings Technology, 2006. **200**(14-15): p. 4153-4165.
14. Dean, J., J.M. Wheeler, and T.W. Clyne, *Use of quasi-static nanoindentation data to obtain stress strain characteristics for metallic materials.* Acta Materialia, 2010. **58**(10): p. 3613-3623.
15. Yan-Ping, C., J. Xiang-Ying, and F. Xi-Qiao, *Geometry independence of the normalized relaxation functions of viscoelastic materials in indentation.* Philosophical Magazine, 2010. **90**(12).
16. Danielewski, M. and B. Wierzba, *Intrinsic diffusivities and Modeling of the diffusion multiples*, in *Diffusion in Solids and Liquids Iii*, A.M.G.E. Ochsner, Editor. 2008. p. 105-112.
17. Zhao, J.C., *The diffusion-multiple approach to designing alloys*, in *Annual Review of Materials Research*. 2005. p. 51-73.
18. Zhao, J.C., M.R. Jackson, and L.A. Peluso, *Mapping of the Nb-Ti-Si phase diagram using diffusion multiples.* Materials Science and Engineering a-Structural Materials Properties Microstructure and Processing, 2004. **372**(1-2): p. 21-27.
19. Zhao, J.C., Z. Xuan, and D.G. Cahill, *High-throughput diffusion multiples intermetallic interdiffusion.* Materials Today, 2005. **8**(10).

20. Branson, J.V., et al., *Heavy Ion Radiation Effects Studies With Ion Photon Emission Microscopy.* AIP Conference Proceedings, 2011. **1336**.
21. Pellish, J.A., et al., *Heavy Ion Microbeam- and Broadbeam-Induced Transients in SiGe HBTs.* Ieee Transactions on Nuclear Science, 2009. **56**(6): p. 3078-3084.
22. Vizkelethy, G., et al., *Time Resolved Ion Beam Induced Current measurements on MOS capacitors using a cyclotron microbeam.* Nuclear Instruments & Methods in Physics Research Section B-Beam Interactions with Materials and Atoms, 2009. **267**(12-13): p. 2185-2188.
23. Hinks, J.A., *A review of transmission electron microscopes with in situ ion irradiation.* Nuclear Instruments & Methods in Physics Research Section B-Beam Interactions with Materials and Atoms, 2009. **267**(23-24): p. 3652-3662.
24. Hinks, J.A., J.A. van den Berg, and S.E. Donnelly, *MIAMI: Microscope and ion accelerator for materials investigations.* Journal of Vacuum Science & Technology A, 2011. **29**(2).
25. Gillespie, G.H. and B.W. Hill, *Open architecture software integration system (OASIS) for the particle beam optics laboratory (PBO Lab).* 2007 IEEE Particle Accelerator Conference, 2007.
26. Kirk, M.A., M.L. Jenkins, and H. Fukushima. *The search for interstitial dislocation loops produced in displacement cascades at 20 K in copper*. in *International Workshop on Basic Aspects of Differences in Irradiation Effects Between FCC, BCC and HCP Metals and Alloys, 15-20 Oct. 1998*
Journal of Nuclear Materials. 2000. Cangas de Onis, Asturias, Spain: Elsevier.
27. Bench, M.W., et al., *Production of amorphous zones in GaAs by the direct impact of energetic heavy ions.* Journal of Applied Physics, 2000. **87**(1): p. 49-56.
28. Jenkins, M.L., et al., *Electron microscope weak-beam imaging of stacking fault tetrahedra: observations and simulations.* Journal of Materials Science, 2006. **41**(14): p. 4445-53.
29. Lei, C.H., et al., *Interface reactions and Kirkendall voids in metal organic vapor-phase epitaxy grown Cu(In,Ga)Se₂ thin films on GaAs.* Journal of Applied Physics, 2006. **100**(11): p. 114915.
30. Battaile, C.C., et al., *The hardness and strength of metal tribofilms: an apparent contradiction between nanoindentation and pillar compression.* Acta Materialia, 2011. **submitted**.

DISTRIBUTION

2 Professor Luke N. Brewer
Department of Mechanical and Aerospace Engineering
Watkins Hall
700 Dyer Road
Naval Postgraduate School
Monterey, CA 93943-5100

1	MS1056	Barney L. Doyle	01111
1	MS1423	Khalid M. Hattar	01111
1	MS0889	Brad L. Boyce	01831
1	MS0889	Thomas E. Buchheit	01814
1	MS1411	Stephen M. Foiles	01814
1	MS1411	Ping Lu	01822
1	MS1423	Blythe G. Clark	01111
1	MS0886	Paul G. Kotula	01822
1	MS0899	RIM-Reports Management	9532 (electronic copy)
1	MS0359	D. Chavez, LDRD Office	1911

Sandia National Laboratories